RSC Advances

PAPER

View Article Online
View Journal | View Issue



Cite this: *RSC Adv.*, 2025, **15**, 43238

# Synthesis of Ag@Co–$NiFe_2O_4$/GO nanocomposites for photocatalysis: X-ray peak profiling, electromagnetic and optical properties

Shahanaz Parvin,[ab] Md. Lutfor Rahman, *[a] Faisal Islam Chowdhury,[b] Bristy Biswas,[a] Md. Farid Ahmed,[a] Moksodur Rahman,[a] Md. Al-Amin,[c] Md. Kamrul Hossain,[b] Shirin Akter Jahan[a] and Nahid Sharmin[a]

This study presents the successful synthesis of $Co_{0.5}Ni_{0.5}Fe_2O_4$ nanoparticles and their composites with silver (Ag) and graphene oxide (GO) using a facile ultrasonic assisted co-precipitation method. Powder X-ray diffraction (PXRD) verified the creation of spinel ferrite structures, integrating Ag nanoparticles and graphene oxide (GO). Crystallite sizes were calculated by detailed X-ray peak profiling using different models including the classical Scherrer method, Munshi–Scherrer method, Williamson–Hall method, size–strain plot method, Halder–Wagner method and conventional Rietveld refinement using GSAS-II software as well as the crystal structure derived from VESTA software. Field emission scanning electron microscopy showed spherical nanoparticles, with energy dispersive X-ray spectroscopy (EDX) verifying the elemental composition. Magnetic analysis showed ferrimagnetic behaviour, with reduced saturation magnetization in Ag and GO-modified samples but increased coercivity for GO-modified system. Optical bandgap analysis *via* UV-DRS indicated bandgaps ranging from 1.95 to 2.03 eV for Ag and GO composites. Dielectric properties were measured, showing a sharp decrease in the dielectric constant at low frequencies, followed by stabilization. Photocatalytic tests revealed that Ag@$Co_{0.5}Ni_{0.5}Fe_2O_4$/GO achieved the highest methylene blue degradation efficiency (96.59%) under visible light, attributed to enhanced electron–hole separation and silver's plasmonic effects. These results suggest that $Co_{0.5}Ni_{0.5}Fe_2O_4$-based nanocomposites, particularly Ag@$Co_{0.5}Ni_{0.5}Fe_2O_4$/GO, have potential for photocatalytic and environmental remediation applications.

Received 2nd March 2025
Accepted 22nd October 2025

DOI: 10.1039/d5ra01475a

rsc.li/rsc-advances



## 1. Introduction

In the dynamic landscape of materials science and nanotechnology, the quest for advanced materials with unique properties has fueled extensive research endeavors. Nanocrystalline materials are three-dimensional solids consisting of nanometer-sized grains or crystallites. Their distinct structure, defined by ultrafine grains and a high density of crystal lattice defects, imparts exceptional fundamental properties. These unique characteristics make nanocrystalline materials promising candidates for developing advanced, next-generation materials well-suited for diverse smart solutions.[1,2]

The development of efficient semiconductor-based photocatalysis has become a promising area of research for environmentally friendly wastewater treatment. Given the negative environmental impacts of rapid industrialization, effective sewage purification is crucial. As reported by the World Bank, the textile sector is responsible for more than 20% of industrial water contamination on a global scale.[3,4] The wastewater generated by this industry is laden with dyes and harmful metals, and inadequate treatment of this effluent presents significant risks to both ecosystems and human well-being.[5–7] Releasing dye-laden wastewater into the environment exacerbates pollution due to chemical processes like hydrolysis and oxidation that take place in sewage systems. Beyond textiles, dyes are also extensively utilized in industries such as leather processing, plastics, and paper production. They are categorized based on their chemical structures into types such as acidic, basic, reactive, metal-complex, disperse, sulfur, phthalocyanine, and triphenylmethane. The environmental impact is further intensified by the textile sector, particularly through the release of wastewater containing positively charged dyes such as methylene blue (MB) and rhodamine B (RhB).[8,9] In recent years, semiconductor materials, particularly binary and ternary metal oxide semiconductors (MOS) and their composites, have made notable progress in wastewater treatment technologies. Significant research efforts have concentrated on the photocatalytic

[a]*Institute of Glass and Ceramic Research and Testing (IGCRT), Bangladesh Council of Scientific and Industrial Research (BCSIR), Dhanmondi, Dhaka-1205, Bangladesh. E-mail: lutforrahman@bcsir.gov.bd; lutforju33@yahoo.com*

[b]*Department of Chemistry, University of Chittagong, Chittagong, Bangladesh*

[c]*BCSIR Rajshahi Laboratories, Bangladesh Council of Scientific and Industrial Research (BCSIR), Rajshahi-6206, Bangladesh*

properties of various binary MOS, such as $TiO_2$, ZnO, and CuO, which have gained attention for their effectiveness over the past several decades.[10–13] Despite this, the widespread use of these photocatalysts in practical applications remains constrained due to challenges such as their large bandgap energy and the rapid recombination of photogenerated electron–hole pairs, which limits their overall efficiency. Ternary semiconductor-based photocatalysts, such as spinel ferrites, are well-known for their promising photocatalytic properties. These materials exhibit high activity, recyclability, stability, and controllable size with smaller particles, making them significant in both basic research and technological advancements in nanoscience and nanotechnology.[14–17]

Magnetic nanoparticles represent an important class of nanomaterials with substantial applications in fields covering disciplines like analytical chemistry, biosensing, and nanomedicine. Nearly a decade and a half has passed since Pankhurst *et al.* published their landmark review on the use of magnetic nanoparticles in biomedical applications.[18] Despite the ongoing challenges in designing magnetic nanoparticles for nanomedicine, these materials continue to attract attention due to their broad range of technological uses. Spinel ferrites are especially notable within magnetic materials due to their distinct chemical, structural, mechanical, and magnetic characteristics. Among these, cobalt ferrite and nickel ferrite are classified as hard and soft magnetic materials, respectively. Hard magnetic materials, such as cobalt ferrite, are characterized by high saturation magnetization and coercivity, while soft ferrites, like nickel ferrite, display lower values for both saturation magnetization and coercivity. These properties make them valuable in various applications depending on the required magnetic behavior.[19,20]

Beyond photocatalysis, Ag-decorated (Co–Ni)$Fe_2O_4$/GO nanocomposites display a synergistic portfolio of structural, magnetic, dielectric and optical features. The spinel lattice permits fine-tuning of crystallite strain (crucial for coercivity engineering), while the Ag core–shell and GO sheets introduce plasmonic hot-spots and high-mobility electron pathways that benefit both electromagnetic shielding and dielectric energy-storage applications. Understanding how these physicochemical attributes co-evolve with photocatalytic activity is therefore essential for device integration in environmental remediation, spintronic logic and microwave absorbers.

Spinel ferrites, represented by the molecular composition $XFe_2O_4$, where X can be elements such as Mg, Ni, Cu, Zn, Fe, or Co, are increasingly recognized as versatile magnetic materials with broad uses.[21] The spinel ferrite structure follows the cubic arrangement $(X)[Y]_2O_4$, where (X) and [Y] refer to ions at the tetrahedral and octahedral positions, respectively, within a face-centered cubic (FCC) anion sub-lattice. In this structure, $X^{2+}$ ions occupy the A-sites, while $Fe^{3+}$ ions are located at the B-sites for $XFe_2O_4$ compounds.

Unlike bulk materials, the nanostructured (Co–Ni)$Fe_2O_4$ framework often exhibits a mixed spinel configuration, with $(Co–Ni)^{2+}$ and $Fe^{3+}$ ions distributed between the A and B-sites.[22,23] As a semiconductor, (Co–Ni)$Fe_2O_4$ stands out due to its low cost, ease of fabrication, and responsiveness to visible light, with a relatively low band gap extending from 1.6 to 2.1 eV. Its abundance of photo-active sites makes (Co–Ni)$Fe_2O_4$ nanoparticles highly promising candidates for photocatalytic applications among all ferrites.[24–27] This material is commercially valuable, demonstrating strong size-dependent magnetic properties, excellent photochemical stability, and robust mechanical durability.[25,28] As a result, (Co–Ni)$Fe_2O_4$ finds extensive use in various domains, including magnetic materials,[29–31] gas sensors,[32] catalysts,[33] photocatalysts,[34–36] lithium-ion battery materials,[37–39] absorbents,[40] and other advanced technologies.

Among graphene oxide (GO) is a versatile nanomaterial that has gained significant attention due to its unique chemical structure, tunable bandgap, and excellent dispersibility. It is widely used as a precursor for graphene-based composites and plays a crucial role in heterogeneous photocatalysis.[41] GO's oxygen-containing functional groups enhance its solubility and provide active sites for surface modifications.[42] Applications of GO span from semiconductor photocatalysts for organic dye degradation[43] to flexible electronics and optoelectronics.[44] Despite its advantages, challenges remain in controlling its reduction process to achieve graphene-like properties while maintaining stability.[45]

In contrast, silver nanoparticles (AgNPs) are highly valued for their remarkable chemical characteristics, biosensing potential, stability, and exceptional conductivity.[46] Within the visible light range, Ag NPs are especially noted for exhibiting local surface plasmon resonance (SPR).[47] The presence of silver on nanoparticles enhances the creation of oxygen vacancies at the surface, offering more active sites for water molecule interaction.[48–50] By attaching silver nano-islands to exposed crystal surfaces, energy levels become aligned, generating an electric field and a Schottky contact between the semiconductor and metal. This arrangement supports directed electron movement, where optimized Schottky barriers enhance the injection and separation of hot electrons. Additionally, the superior conductivity of silver plays a crucial role in facilitating a Z-scheme electron mediator process by introducing a tertiary semiconductor material.[51]

Wastewater purification *via* photocatalytic degradation is typically conducted using ultraviolet (UV) light, with mercury and xenon lamps being the most common UV light sources.[52–54] However, these lamps pose several challenges, including high energy consumption, the presence of toxic mercury, operational difficulties, and costly installation. These limitations have significantly hindered the advancement of photocatalytic reactors and the widespread application of photocatalytic processes.[55] To address these issues, researchers have increasingly turned to more energy-efficient alternatives, such as sunlight, LEDs and halogen lamps, as light sources for photocatalysis.[56] In our study, we selected halogen lamps as the light source to evaluate the activity of our composites.

## 2. Materials and methodology

### 2.1 Materials

The starting materials employed in the synthesis of cobalt–nickel ferrite and its nanocomposites include $Fe(NO_3)_3 \cdot 9H_2O$,

$Ni(NO_3)_2 \cdot 6H_2O$, $Co(NO_3)_2 \cdot 6H_2O$, $C_6H_5Na_3O_7 \cdot 2H_2O$, $AgNO_3$, NaOH, graphite, $H_2SO_4$, $KMnO_4$, $NaNO_3$, HCl, and $H_2O_2$. The materials were of excellent purity and supplied by Merck, Germany, except for $AgNO_3$, which was obtained from Wako, China. Deionized (DI) water was utilized throughout the experimental process.

### 2.2 Preparation of graphene oxide

In the typical preparation process, 3.5 g of graphite and 1.75 g of sodium nitrate were dispersed in 100 mL of concentrated sulfuric acid (98%). The dispersion was cooled to approximately 5 °C using an ice bath and stirred for 2.5 hours. Over the next 2.5 hours, 12 g of potassium permanganate was gradually added while stirring continued for an additional 2 hours. The cooling bath was subsequently taken away, allowing the mixture to gradually return to ambient temperature. Following that approximately 120 mL of distilled water was gradually introduced over the course of one hour, during which gas was liberated, and the temperature was elevated to about 90 °C using a water bath. Upon achieving this temperature, an additional 320 mL of water was incorporated, and the mixture was continuously stirred for 1.5 hours, yielding a brown suspension. The mixture was then treated with 30% hydrogen peroxide ($H_2O_2$), and approximately 4 liters of warm distilled water were added to further dilute the suspension. The precipitate was left to settle under the force of gravity for 24 hours, after which the clear liquid on top was carefully decanted. To eliminate any residual manganese and sulfate ions, 2 M hydrochloric acid (HCl) was introduced into the mixture. The resulting suspension was thoroughly rinsed multiple times with distilled water and subjected to high-speed centrifugation until the pH stabilized at neutral (~7). Finally, graphene oxide (GO) was obtained through filtration and stored in a vacuum desiccator with silica gel for several days before it was used for characterization and composite formation (Fig. 1).[57]

### 2.3 Preparation of $Ag@Co_{0.5}Ni_{0.5}Fe_2O_4$/GO nanocomposite

$Ag@Co_{0.5}Ni_{0.5}Fe_2O_4$ nanoparticles were synthesized *via* the co-precipitation technique. In a typical procedure, specific amounts of $Co(NO_3)_2 \cdot 6H_2O$ (0.5 M), $Ni(NO_3)_2 \cdot 6H_2O$ (0.5 M), and $Fe(NO_3)_2 \cdot 9H_2O$ (0.5 M) were individually dissolved in deionized (DI) water at a mole ratio of 0.5 : 0.5 : 2. These solutions were then mixed in a beaker and stirred continuously using a magnetic stirrer for 30 minutes. Following this, an aqueous NaOH (5 M) solution was gradually added to the mixture until the pH reached 12. Subsequently, $AgNO_3$ (0.5 M) and $C_6H_5N_3O_7 \cdot 2H_2O$ (0.5 M), in an equivalent molar ratio (1 : 1) to the ferrite, were introduced into the solution. The resulting mixture was heated at 90 °C for 1 hour. The solution was then rinsed with DI water and centrifuged until the pH stabilized at 7. The material was dried in an oven at 120 °C for 12 hours. Finally, the dried product was calcined at 800 °C for 3 hours, with a heating rate of 3 °C $min^{-1}$, to obtain $Ag@Co_{0.5}Ni_{0.5}Fe_2O_4$ nanoparticles. For the preparation of the ternary composite, 30 wt% of graphene oxide (GO) and 3 g of $Ag@Co_{0.5}Ni_{0.5}Fe_2O_4$ were dispersed in 100 mL of DI water and subjected to ultrasonication for 120 minutes to ensure uniform dispersion. The resulting mixture was dried in an oven and subsequently ground into a fine powder to produce the final composite, $Ag@Co_{0.5}Ni_{0.5}Fe_2O_4$/GO. $Co_{0.5}Ni_{0.5}Fe_2O_4$/GO synthesis using the same manner absence Ag. The synthesis of $Co_{0.5}Ni_{0.5}Fe_2O_4$/GO was carried out in the same manner, but without the addition of Ag. The schematic diagram illustrating the synthesis process is shown in Fig. 2.

### 2.4 Characterizations

The synthesized nanocomposites were characterized for their phase composition using a (Rigaku SmartLab SE) powder X-ray diffractometer with high-intensity Cu Kα radiation ($\lambda = 1.5406$ Å) over a $2\theta$ range of 10–80°. Surface morphology was investigated using a (JSM-IT-800, JEOL, Japan) field emission scanning

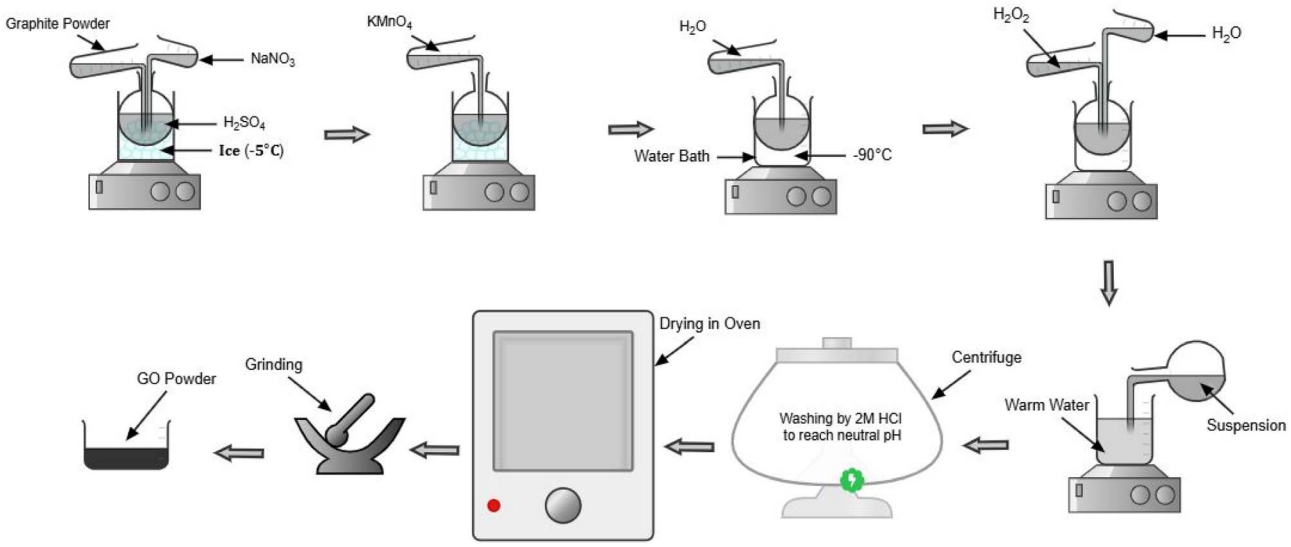


Fig. 1 Graphical representation of the GO preparation method.

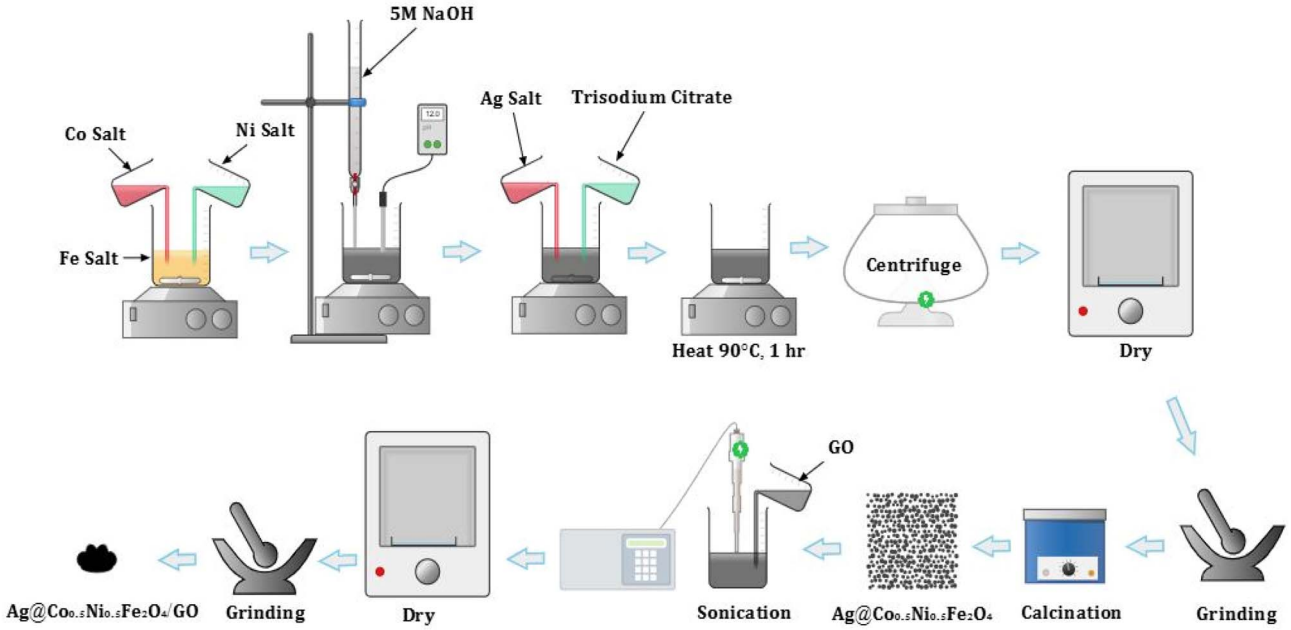


Fig. 2 Synthesis of Ag@$Co_{0.5}Ni_{0.5}Fe_2O_4$/GO nanocomposite.

electron microscopy (FE-SEM). Magnetic properties were studied at room temperature with a Vibrating Sample Magnetometer (VSM-8600, Lakeshore, USA) under an applied magnetic field up to 20 kOe. Dielectric and electrical properties were measured using an impedance analyzer (65120B, Wayne Kerr Electronics, UK) across a frequency range of 100 Hz to 20 MHz at room temperature, employing a dielectric measurement fixture. For sample preparation, the powders were homogenized with a 5% aqueous solution of polyvinyl alcohol using a mortar and pestle, then pressed into 10 mm diameter pellets under a pressure of 5 kN. The pellets were calcined at 300 °C to remove the binder by evaporation.

## 3. Result and discussion

### 3.1 X-ray diffraction (XRD) analysis

Fig. 3 presents the powder X-ray diffraction (PXRD) patterns for the samples synthesized in this study. The diffraction signal recorded at $2\theta = 11.8°$ corresponds to the (001) diffraction plane, which validates the formation of graphene oxide (GO). Additionally, the crystalline quality and phase purity of the $Co_{0.5}Ni_{0.5}Fe_2O_4$ nanomaterials were evaluated through their PXRD patterns, displaying distinct peaks at approximately $2\theta$ values of 18.1°, 30.2°, 35.5°, 37.3°, 43.2°, 57.2°, 62.8°, 74.3°, and 75.7°. These peaks correspond to the (111), (220), (311), (222),

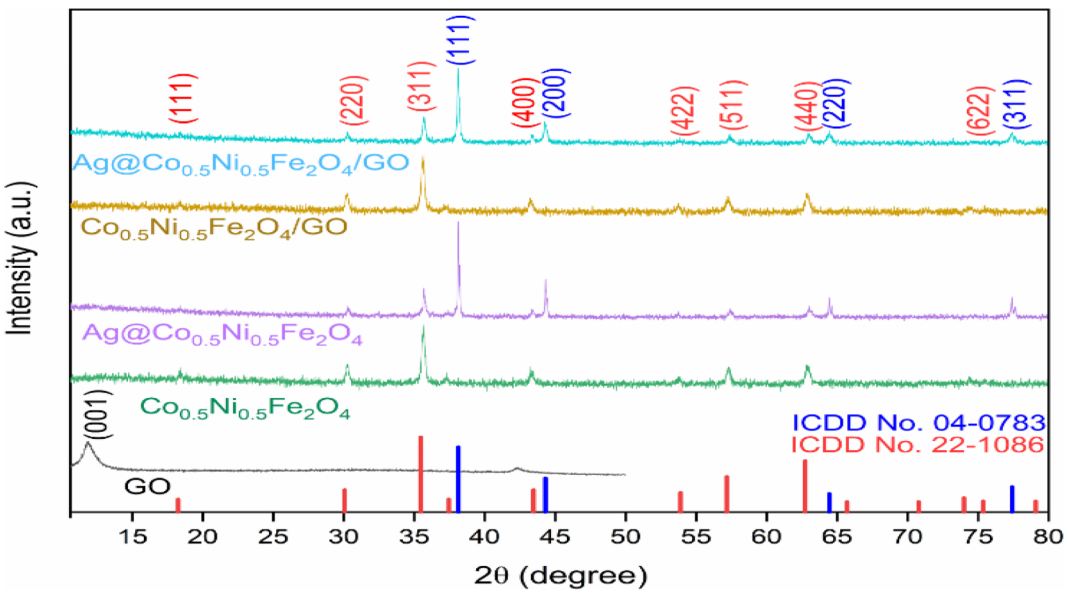


Fig. 3 PXRD pattern of GO, $Co_{0.5}Ni_{0.5}Fe_2O_4$, Ag@$Co_{0.5}Ni_{0.5}Fe_2O_4$, $Co_{0.5}Ni_{0.5}Fe_2O_4$/GO, and Ag@$Co_{0.5}Ni_{0.5}Fe_2O_4$/GO composites.

(400), (511), (422), (440), and (622) crystal planes, respectively. The observed peaks are align with the reference data (ICDD no. 22-1086) for the face-centered cubic structure characteristic of spinel ferrite.[58] In the case of the Ag@$Co_{0.5}Ni_{0.5}Fe_2O_4$/GO samples, additional diffraction peaks associated with Ag nanoparticles were identified in Fig. 3. The Bragg reflection peaks at 2$\theta$ values of 38.1°, 44.3°, 64.42°, and 77.45° correspond to the (111), (200), (220), and (311) planes of pure silver, in accordance with the face-centered cubic structure (ICDD no. 04-0783).[59] While all reflection planes pertaining to $Co_{0.5}Ni_{0.5}Fe_2O_4$ are distinctly observed, the reflection planes for GO in the $Co_{0.5}Ni_{0.5}Fe_2O_4$/GO composite are not detectable. The GO content in the composites is considerably lower than that of the dominant spinel ferrite, $Co_{0.5}Ni_{0.5}Fe_2O_4$. This low concentration weakens the diffraction signals from GO, often rendering them undetectable by the XRD instrument. Additionally, the layered materials are extensively dispersed within the ferrite matrix, resulting in significant exfoliation. This high dispersion disrupts the long-range crystalline order necessary for pronounced XRD peaks, leading to the reduction or disappearance of GO's characteristic peaks.[60,61]

**3.1.1 From PXRD data, the peak profile analysis carried out by following parameters.** The average crystallite sizes were determined using several techniques, including the Classical Scherrer (CS) equation,[62] Munshi–Scherrer (M–S) method,[62] Williamson–Hall (W–H) analysis,[62] Halder–Wagner (HW) approach,[57] and the Size–Strain Plot (SSP) method.[35] These methods are illustrated in Fig. 4–7, and the corresponding results are summarized in Table 1.

*3.1.1.1 Classical Scherrer (CS) method.* The crystallite sizes were calculated utilizing the conventional Scherrer method ($D_{C\text{-}S}$),[63] which is governed by the following equation:

$$D_{C\text{-}S} = \frac{0.9\lambda}{(\beta_{hkl} \cos\theta)} \quad (1)$$

In this equation, $\lambda$ signifies the wavelength of the X-ray used, while $\beta_{hkl}$ refers to the full width at half maximum (FWHM) of the diffraction peak intensity corresponding to the specific Miller indices. Additionally, $\theta$ represents the Bragg angle at which the diffraction occurs.

*3.1.1.2 Munshi–Scherrer (M–S) method.* The Munshi–Scherrer equation is derived by rearranging eqn (1) and applying a logarithmic transformation to both sides.[62]

$$\ln\ \beta_{hkl} = \ln\left(\frac{0.9\lambda}{D_{M-S}}\right) + \ln\left(\frac{1}{\cos\theta}\right) \quad (2)$$

$$D_{M-S} = \frac{0.9\lambda}{e^{\text{intercept}}} \quad (3)$$

By employing eqn (2) and (3), the crystallite size was obtained from the intercept of a linear graph, where ln(1/cos $\theta$) is represented on the *X*-axis and ln $\beta$ is displayed on the *Y*-axis.

*3.1.1.3 Williamson–Hall (W–H) method.* The average crystallite size was also estimated using the Williamson–Hall (W–H) model.[62] In the W–H framework the observed peak width $\beta$ (in radians) is the vector sum of size-induced broadening $K\lambda/D$ and micro-strain broadening $4\varepsilon \tan\theta$:

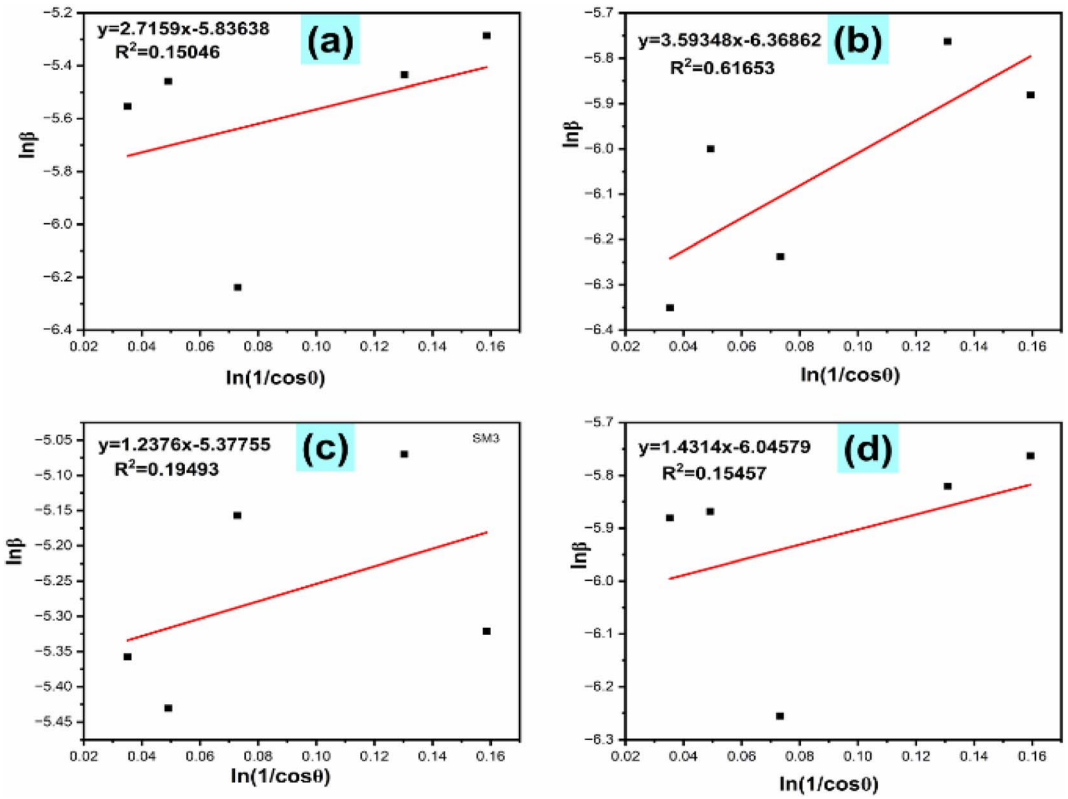


Fig. 4 Munshi–Scherrer plots of (a) $Co_{0.5}Ni_{0.5}Fe_2O_4$, (b) Ag@$Co_{0.5}Ni_{0.5}Fe_2O_4$, (c) $Co_{0.5}Ni_{0.5}Fe_2O_4$/GO, and (d) Ag@$Co_{0.5}Ni_{0.5}Fe_2O_4$/GO.

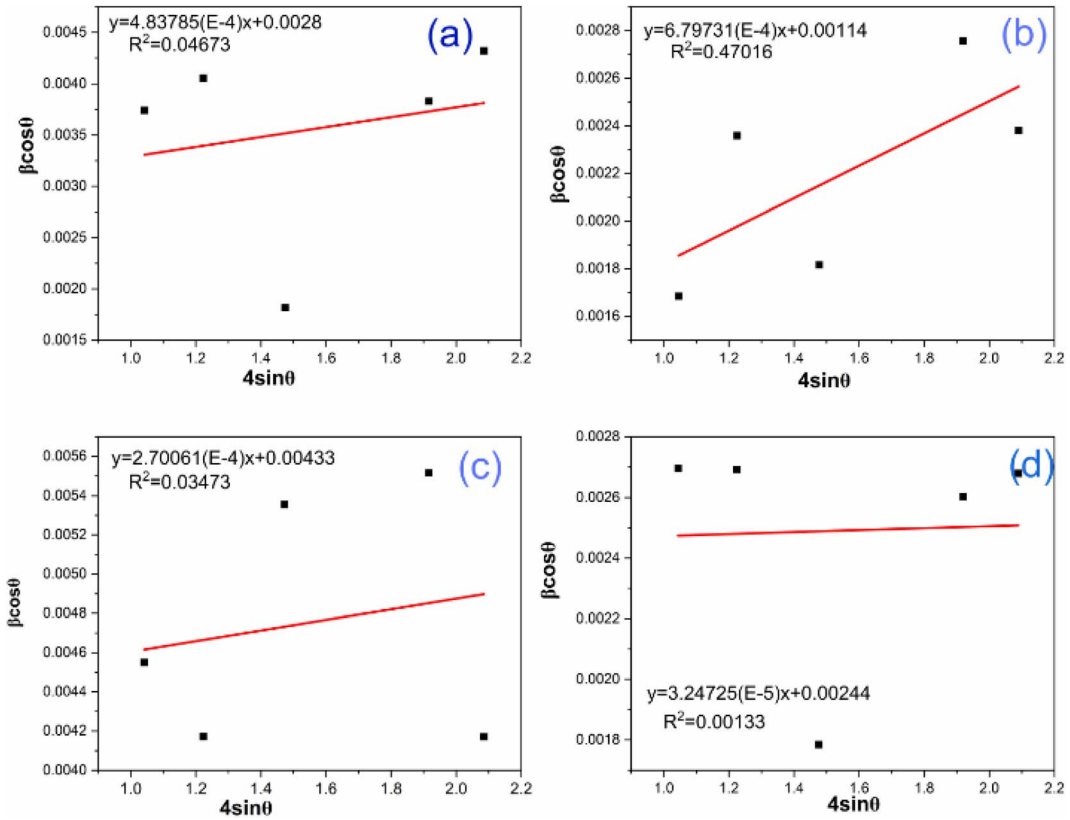


Fig. 5 Williamson–Hall plots of (a) $Co_{0.5}Ni_{0.5}Fe_2O_4$, (b) $Ag@Co_{0.5}Ni_{0.5}Fe_2O_4$, (c) $Co_{0.5}Ni_{0.5}Fe_2O_4$/GO, and (d) $Ag@Co_{0.5}Ni_{0.5}Fe_2O_4$/GO.

$$\beta_{hkl} \cos\theta = \frac{0.9\lambda}{D_{W-H}} + 4\varepsilon \sin\theta \quad (4)$$

where $K = 0.9$ (shape factor), $\lambda = 1.5406$ Å (Cu Kα), $D$ is the volume-weighted crystallite size, $\varepsilon$ the lattice strain, and $\theta$ the Bragg angle. Plotting $\beta \cos\theta$ *versus* $4 \sin\theta$ gives a straight line whose intercept estimates $D$ and whose slope yields $\varepsilon$. This simultaneous deconvolution highlights the strain relaxation imparted by Ag decoration and/or GO interlayers. Using eqn (5), the crystallite size was calculated from the intercept as:

$$D_{W-H} = \frac{0.9\lambda}{\text{intercept}} \quad (5)$$

*3.1.1.4 Size–strain plot (SSP) method.* The Size–Strain Plot (SSP) model was also employed to evaluate the crystallite size, as described by eqn (6) and (7).[35]

$$(D_{hkl}\beta_{hkl} \cos\theta)^2 = \frac{K\lambda}{D(d_{hkl}{}^2\beta_{hkl} \cos\theta)} + \left(\frac{\varepsilon}{2}\right)^2 \quad (6)$$

$$D_{SSP} = \frac{0.9\lambda}{\text{slope}} \quad (7)$$

The crystallite size was determined from the slope of the fitted line, which is obtained by plotting $(d\beta \cos\theta)^2$ against $(d^2\beta \cos\theta)$.

*3.1.1.5 Halder–Wagner method.* The Halder–Wagner model is another method used to accurately determine crystallite size, as expressed in eqn (8).[57]

$$\left(\frac{\beta_{hkl}}{\tan\theta}\right)^2 = \left(\frac{K\lambda}{D_{H-W}}\right) \times \left(\frac{\beta_{hkl}}{\tan\theta \times \cos\theta}\right) + 16\varepsilon^2 \quad (8)$$

A linear fit is created by plotting $(\beta_{hkl}/\tan\theta)^2$ against $(\beta_{hkl}/\tan\theta \times \cos\theta)$, and the slope of the resulting graph provides the Halder–Wagner crystallite size.

Crystallite size estimations using multiple methodologies, including the Scherrer equation, Williamson–Hall (W–H) method, Size–Strain Plot (SSP), and Halder–Wagner (H–W) approach, provided a comprehensive understanding of the structural characteristics. The slight variations in crystallite size across different models highlight the limitations of traditional peak broadening methods in precisely quantifying nanoscale particle sizes. Notably, the SSP and H–W techniques yielded more reliable results, as evidenced by their higher regression coefficients ($R^2$) of 0.96814, 0.78402, 0.95021, and 0.98324 for the samples $Co_{0.5}Ni_{0.5}Fe_2O_4$, $Ag@Co_{0.5}Ni_{0.5}Fe_2O_4$, $Co_{0.5}Ni_{0.5}Fe_2O_4$/GO, and $Ag@Co_{0.5}Ni_{0.5}Fe_2O_4$/GO, respectively,[52] suggesting that strain effects and instrumental broadening were effectively accounted for. Notably, it was observed that the crystallite size of the ferrite nanoparticles in the Ag-doped $Co_{0.5}Ni_{0.5}Fe_2O_4$ is larger than that of the unmodified $Co_{0.5}Ni_{0.5}Fe_2O_4$ nanoparticles.[64]

Lattice constant '$a$' was calculated using eqn (9)

$$a = d_{hkl}\sqrt{h^2 + k^2 + l^2} \quad (9)$$

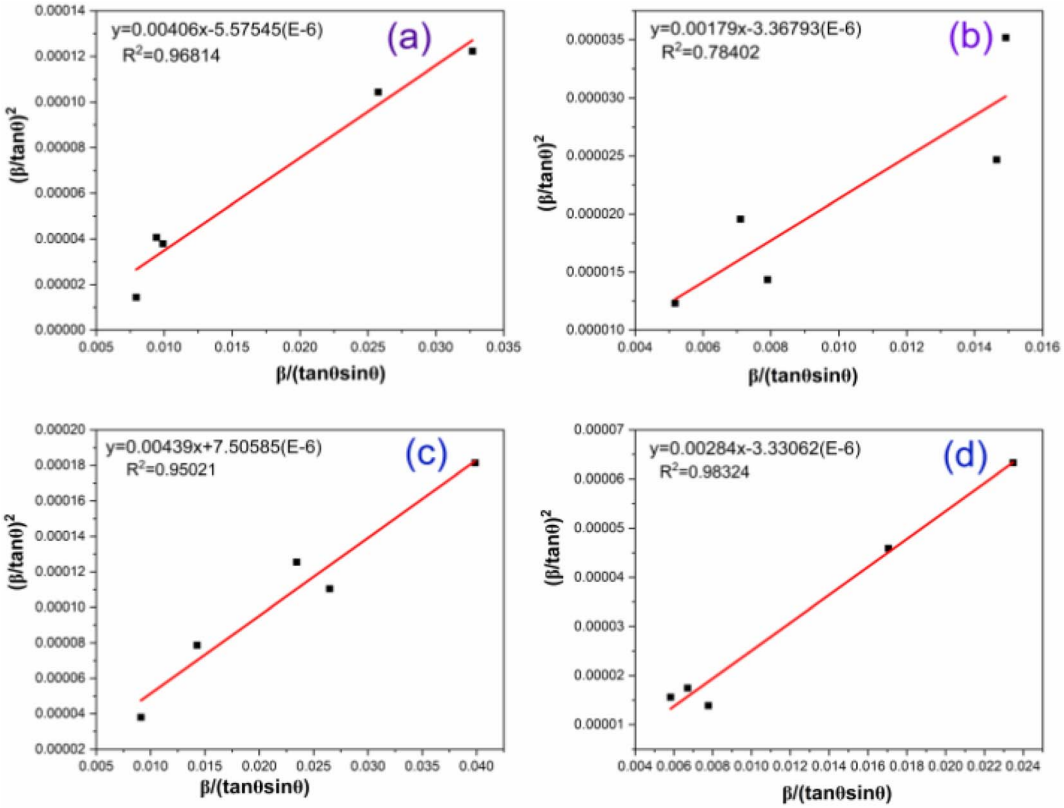


Fig. 6 Size–strain plots of (a) $Co_{0.5}Ni_{0.5}Fe_2O_4$, (b) Ag@$Co_{0.5}Ni_{0.5}Fe_2O_4$, (c) $Co_{0.5}Ni_{0.5}Fe_2O_4$/GO, and (d) Ag@$Co_{0.5}Ni_{0.5}Fe_2O_4$/GO.

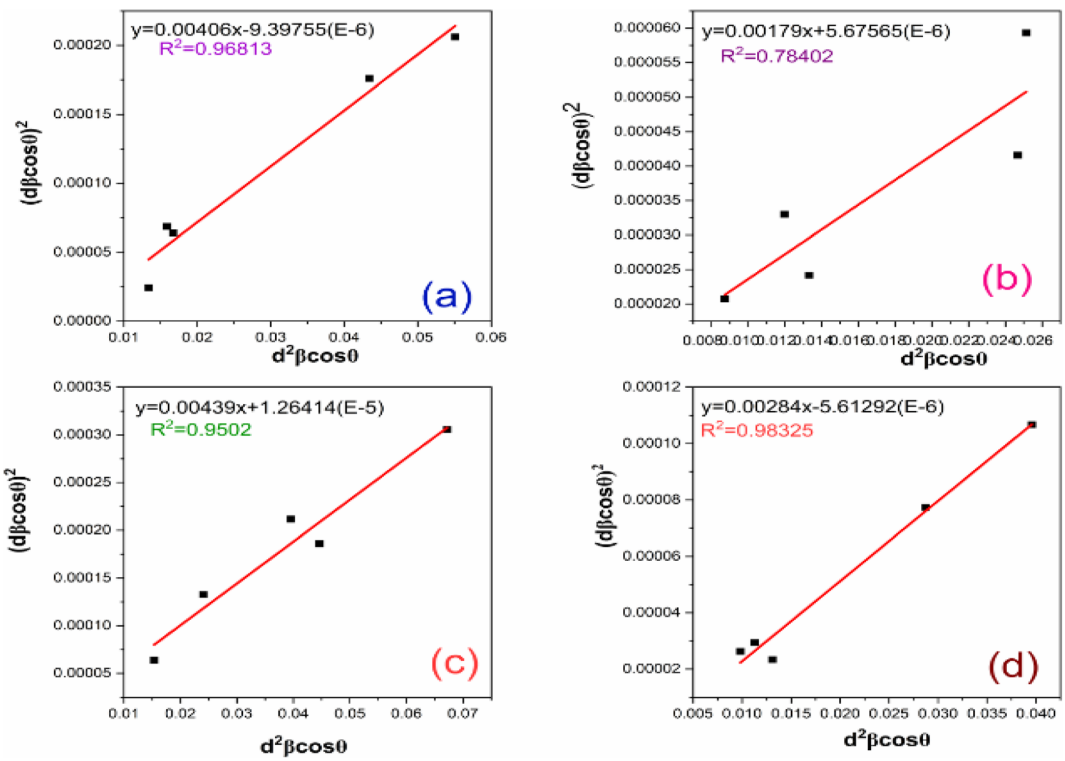


Fig. 7 Halder–Wagner plots of (a) $Co_{0.5}Ni_{0.5}Fe_2O_4$, (b) Ag@$Co_{0.5}Ni_{0.5}Fe_2O_4$, (c) $Co_{0.5}Ni_{0.5}Fe_2O_4$/GO, and (d) Ag@$Co_{0.5}Ni_{0.5}Fe_2O_4$/GO.

Table 1 Summary of crystallite size, lattice parameter, strain, and surface area of the materials

| | Crystallite size (nm) | | | | | Lattice parameter | | | |
|---|---|---|---|---|---|---|---|---|---|
| Sample no. | $D_{C\text{-}S}$ | $D_{M\text{-}S}$ | $D_{W\text{-}H}$ | $D_{H\text{-}W}$ | $D_{SSP}$ | $a$ (Å) | $V$ (Å$^3$) | $\varepsilon$ ($10^{-4}$) | $S$ (m$^2$ g$^{-1}$) |
| $Co_{0.5}Ni_{0.5}Fe_2O_4$ | 36.6 | 47.5 | 49.5 | 44.2 | 44.2 | 8.35922 | 584.11 | 4.33 | 48.49 |
| $Ag@Co_{0.5}Ni_{0.5}Fe_2O_4$ | 55.4 | 80.9 | 121.6 | 77.5 | 77.5 | 8.33965 | 580.02 | 2.74 | 31.92 |
| $Co_{0.5}Ni_{0.5}Fe_2O_4$/GO | 25.5 | 30 | 32 | 31.6 | 31.6 | 8.35557 | 583.35 | 5.69 | 69.38 |
| $Ag@Co_{0.5}Ni_{0.5}Fe_2O_4$/GO | 48.1 | 58.6 | 56.8 | 48.8 | 48.8 | 8.34794 | 581.75 | 2.99 | 36.82 |

The surface area and lattice strain ($\varepsilon$) of the prepared sample were calculated using eqn (10) and (11).[65]

$$S = \frac{6}{D_{C\text{-}S} \times Q_X} \tag{10}$$

$$\varepsilon = \beta_{hkl}/\tan\theta \tag{11}$$

The bulk density ($Q_b$) was determined based on the parameters of the pellets using the following equation.[57]

$$Q_b = m/\pi r^2 t \tag{12}$$

where $m$, $r$, and $t$ represent the weight, radius, and thickness of the pellets, respectively.

The percentage porosity ($P$) of the samples was calculated using the following formula:

$$P = 1 - (\text{bulk density/X-ray density}) \tag{13}$$

where the X-ray density ($Q_X$) was obtained from the Rietveld refinement.

Using PXRD data, various parameters related to tetrahedral (A-sites) and octahedral (B-sites) configurations, such as ionic radii ($Ir_A$, $Ir_B$), bond lengths ($BL_{A\text{–}O}$, $BL_{B\text{–}O}$), and hopping lengths ($HL_A$, $HL_B$), were also calculated by applying eqn (14) and (15), (16) and (17), and (18) and (19), respectively.[66–68]

$$Ir_A = \left(u - \frac{1}{4}\right)a\sqrt{3} - r(O^{2-}) \tag{14}$$

$$Ir_B = \left(\frac{5}{8} - u\right)a - r(O^{2-}) \tag{15}$$

$$\text{Bond length, } BL_{A\text{–}O} = \left(u - \frac{1}{4}\right)a\sqrt{3} \tag{16}$$

$$\text{Bond length, } BL_{B\text{–}O} = \left(\frac{5}{8} - u\right)a \tag{17}$$

$$HL_A = \frac{a\sqrt{3}}{4} \tag{18}$$

$$HL_B = \frac{a\sqrt{2}}{4} \tag{19}$$

Here, $a$ represents the lattice constant, $r(O^{2-})$ denotes the radius of the oxygen ion (0.135 nm), and $u$ is the oxygen ion parameter (0.375) for an ideal spinel ferrite.

The dislocation density ($\delta$) was calculated from the crystallite size values using the relationship

$$\delta = 1/D^2 \tag{20}$$

It is well-established that dislocation density is indirectly related to crystallite size. Consequently, in this case, the dislocation density exhibited a random variation similar to that observed in the crystallite size values.[69]

The crystalline percentage was assessed through the XRD deconvolution approach, utilizing OriginPro 24 software to quantify the integrated area of the crystalline peaks alongside the total integrated area, which encompasses both crystalline and amorphous contributions beneath the XRD peaks. The calculation is performed using the following formula:

$$\text{Crystallinity } (\%) = \frac{S_c}{S_t} \times 100 \tag{21}$$

In this context, $S_c$ refers to the integrated area corresponding to the crystalline peaks, whereas $S_t$ indicates the total integrated area beneath the XRD peaks.[70]

The lattice constants and cell volumes were extracted from the powder X-ray diffraction (PXRD) data. The determined cell constants for the $Co_{0.5}Ni_{0.5}Fe_2O_4$, $Ag@Co_{0.5}Ni_{0.5}Fe_2O_4$, $Co_{0.5}Ni_{0.5}Fe_2O_4$/GO, and $Ag@Co_{0.5}Ni_{0.5}Fe_2O_4$/GO samples were found to be 8.35922 Å, 8.33965 Å, 8.35557 Å, and 8.34794 Å, respectively. Correspondingly, the cell volumes were calculated as 584.11 Å$^3$, 580.02 Å$^3$, 583.35 Å$^3$, and 581.75 Å$^3$. These lattice parameters closely align with the standard values (ICDD no. 22-1086), which are recorded as 8.3479 Å and 581.75 Å$^3$. Furthermore, the surface area ($S$) and lattice strain ($\varepsilon$) were derived from the PXRD data, as summarized in Table 1. The percentage porosity ($P$) of the samples was estimated using X-ray density measurements. The table also includes values for bulk density, dislocation density, and percentage crystallinity. Additionally, several tetrahedral and octahedral parameters of the spinel ferrite were obtained from the PXRD data to assess the influence of graphene and silver on the $Co_{0.5}Ni_{0.5}Fe_2O_4$ nanoparticles, as outlined in Table 2.[58]

Rationale for multiple peak-broadening models: a single line-profile method seldom captures the full microstructural picture. The classical Scherrer equation yields a quick first estimate but conflates size and strain broadening. Williamson–Hall separates the two contributions assuming isotropic strain, whereas the Munshi–Scherrer linearisation improves statistical robustness for broad peaks. Size–strain plot and Halder–Wagner further account for anisotropic broadening and

Table 2 Summary of bulk density, porosity, ionic radii, bond length, hopping length, dislocation density and crystallinity of the obtained materials

| Sample id | Bulk-ray density ($\rho_b$) (g cm$^{-3}$) | Porosity, $P$ (%) | Ionic radii (nm) | | Bond length (nm) | | Hoping length (nm) | | Dislocation density (lines per m$^2$) $\times 10^{14}$ | Crystallinity (%) |
|---|---|---|---|---|---|---|---|---|---|---|
| | | | $Ir_A$ | $Ir_B$ | $BL_{A-O}$ | $BL_{B-O}$ | $HL_A$ | $HL_B$ | | |
| $Co_{0.5}Ni_{0.5}Fe_2O_4$ | 3.364 | 37 | 0.04598 | 0.07398 | 0.18109 | 0.2089 | 0.3619 | 0.2955 | 7.48 | 85.84 |
| $Ag@Co_{0.5}Ni_{0.5}Fe_2O_4$ | 4.212 | 23 | 0.04555 | 0.07349 | 0.18056 | 0.2084 | 0.3611 | 0.2948 | 3.26 | 87.45 |
| $Co_{0.5}Ni_{0.5}Fe_2O_4$/GO | 2.667 | 51 | 0.04590 | 0.07389 | 0.18090 | 0.2089 | 0.3618 | 0.2954 | 15.34 | 92.79 |
| $Ag@Co_{0.5}Ni_{0.5}Fe_2O_4$/GO | 2.937 | 45 | 0.04573 | 0.07369 | 0.18073 | 0.2087 | 0.3614 | 0.2951 | 4.3 | 95.41 |

instrumental convolution; their higher $R^2$ values (0.95–0.98) in our data underscore their reliability. Using this multi-model ensemble therefore cross-validates crystallite size while revealing latent strain and anisotropy effects that single models overlook.

Conventional Rietveld refinement was conducted to precisely evaluate the crystal structure and lattice parameters of the PXRD patterns, utilizing the space groups *Fd3m* for $Co_{0.5}Ni_{0.5}Fe_2O_4$ and *Fm3m* for silver (Ag).[71] The refined PXRD patterns, along with the resulting crystal structures derived from the refinement data, are presented in Fig. 8 and 9, respectively, as obtained through VESTA software. The quality of the empirical data fitting was determined using several metrics, including the unweighted profile $RF^2$-factor, weighted profile *R*-factor (RF), expected *R*-factor ($R_{exp}$), and Goodness of Fit (GoF), all of which were required to be below 10%.[72] The parameters from the Rietveld refinement, along with the lattice constants for the synthesized samples, are compiled in Table 3. Furthermore, a polyhedral representation of the $Co_{0.5}Ni_{0.5}Fe_2O_4$ spinel structure, created with VESTA software, is displayed in Fig. 9. The lattice parameters extracted from Rietveld refinement closely matched reference values, indicating minimal structural distortion upon Ag and GO incorporation. However, the slight reduction in lattice constant for the $Ag@Co_{0.5}Ni_{0.5}Fe_2O_4$/GO composite suggests potential lattice contraction due to Ag incorporation, which may introduce additional strain. The dislocation density, which is inversely proportional to crystallite size, followed an expected trend, with the Ag-containing composites exhibiting lower defect densities, implying an improvement in crystallinity.

### 3.2 Morphological and compositional analysis of elemental constituents

The morphological features and particle size distribution of $Co_{0.5}Ni_{0.5}Fe_2O_4$ and its modified counterparts were investigated using Field Emission Scanning Electron Microscopy (FE-SEM). The resulting FE-SEM micrographs are displayed in Fig. 10, and recorded particle diameters, as summarized in Table 4, exhibit a systematic variation in response to both Ag incorporation and GO incorporation. The pristine $Co_{0.5}Ni_{0.5}Fe_2O_4$ nanoparticles demonstrated an average diameter of 50.57 nm, indicative of well-defined, nanoscale features with minimal agglomeration. However, upon Ag incorporation ($Ag@Co_{0.5}Ni_{0.5}Fe_2O_4$), a slight increase in particle size to 51.76 nm was observed. This enlargement can be attributed to the incorporation of Ag nanoparticles, which induce localized lattice strain and facilitate particle growth due to surface diffusion effects. Such trends are consistent with previous studies on noble metal-doped ferrites, where Ag incorporation has been reported to increase grain size due to its impact on nucleation kinetics and crystallite coarsening during synthesis.[73,74]

In contrast, the addition of graphene oxide (GO) into the $Co_{0.5}Ni_{0.5}Fe_2O_4$ matrix resulted in a size reduction to 46.60 nm ($Co_{0.5}Ni_{0.5}Fe_2O_4$/GO), suggesting that GO restricts nanoparticle growth during the synthesis process. This reduction in size is likely driven by GO-induced confinement effects, where the high surface area of GO acts as a barrier to grain growth, thereby limiting coalescence during crystallization.[75] Additionally, the oxygen-containing functional groups on GO sheets may enhance interfacial interactions, leading to reduced mobility of the ferrite particles and further inhibiting growth. A more pronounced effect was observed in the $Ag@Co_{0.5}Ni_{0.5}Fe_2O_4$/GO nanocomposite, where the particle diameter significantly decreased to 37.50 nm. The combined influence of Ag incorporation and GO interaction appears to exert a synergistic effect, further restricting particle size. The observed trend suggests that GO nanosheets effectively suppress ferrite grain growth, and the presence of Ag facilitates defect formation, which may impede particle aggregation and accelerate nucleation, leading to finer nanoparticles.[75,76]

The progressive decrease in particle size with GO modification has crucial implications for the magnetic and electrochemical behavior of these nanocomposites. A smaller particle size enhances the surface-to-volume ratio, which can influence interfacial charge transfer, catalytic efficiency, and exchange interactions in magnetic systems. Additionally, size reduction enhances coercivity, as smaller particles exhibit greater shape anisotropy, further reinforcing the correlation between morphology and magnetic properties.[75–79] The FE-SEM analysis confirms that Ag and GO serve distinct roles in structural evolution, with Ag incorporation favoring particle coarsening, while GO incorporation restricts growth and induces surface modification effects. This fine-tuning of nanoparticle size provides a strategic pathway for optimizing performance in spintronics, energy storage, and high-frequency magnetic applications.[79]

The FE-SEM-determined particle size was larger than the crystallite size (C–S plot method) due to crystallite aggregation,

 

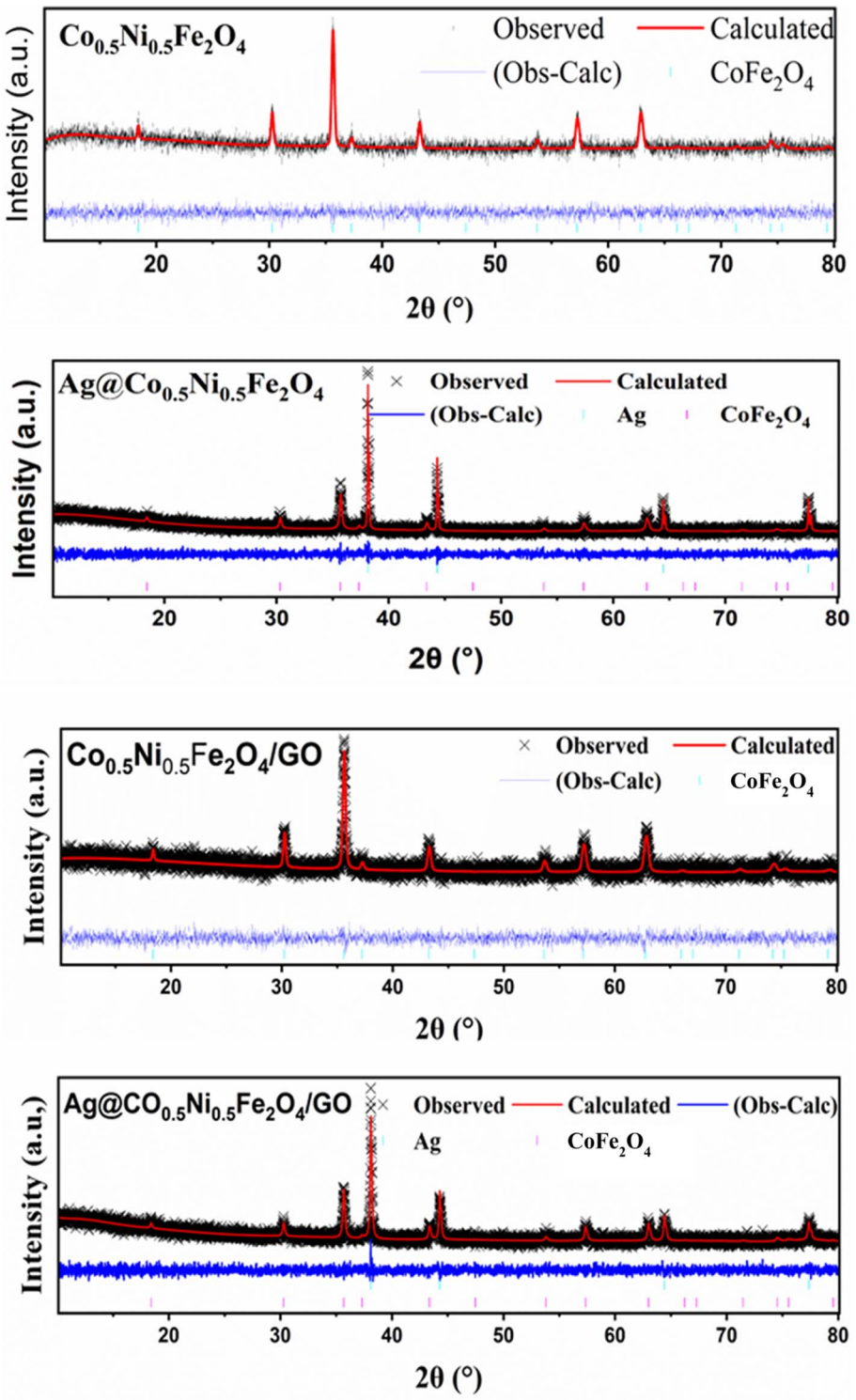


Fig. 8 Refined PXRD pattern of $Co_{0.5}Ni_{0.5}Fe_2O_4$, $Ag@Co_{0.5}Ni_{0.5}Fe_2O_4$, $Co_{0.5}Ni_{0.5}Fe_2O_4$/GO and $Ag@Co_{0.5}Ni_{0.5}Fe_2O_4$/GO.

grain boundary diffusion, and synthesis-induced growth. While the C–S plot estimates the coherent diffracting domains, FE-SEM accounts for physical particle size, leading to this discrepancy.[60,75,76]

EDX analysis (Table 5) confirms the successful incorporation of Ag and GO. The pristine $Co_{0.5}Ni_{0.5}Fe_2O_4$ maintained a Fe : Co : Ni ratio of 1.95 : 0.56 : 0.50, aligning with the expected spinel structure. However, Ag doping ($Ag@Co_{0.5}Ni_{0.5}Fe_2O_4$) increased O content (39.68%) while reducing Fe, Co, and Ni levels, suggesting partial oxidation and cation redistribution. The presence of Ag (11.66%) indicates its integration into the ferrite matrix. For GO-modified composites, C (13.07%) and O

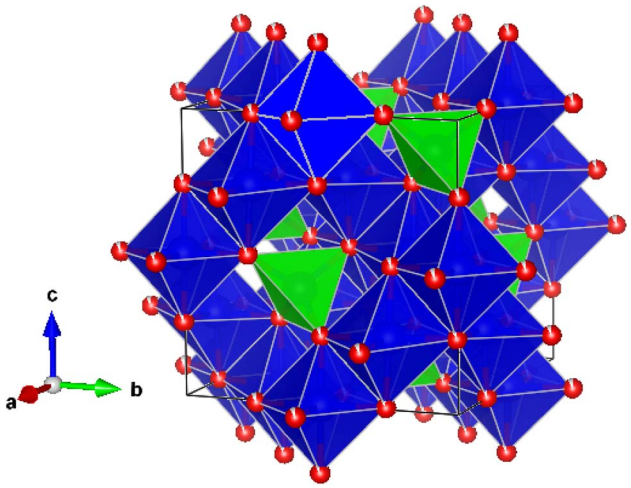


Fig. 9 The crystal structure of $Co_{0.5}Ni_{0.5}Fe_2O_4$, derived from the refined data, was visualized using the VESTA software package.

(26.70%) content confirmed GO integration, which restricted grain growth and influenced magnetic/electronic properties. The $Ag@Co_{0.5}Ni_{0.5}Fe_2O_4/GO$ composite exhibited higher Ag (14.11%) and enhanced C/O levels, suggesting GO stabilizes Ag nanoparticles, preventing agglomeration.[60] These compositional changes impact superexchange interactions, charge transfer, and anisotropy, crucial for magnetic and electronic applications (Fig. 11).

### 3.3 Magnetic properties analysis

The saturation magnetization ($M_s$) in relation to the external magnetic field ($H$) for $Co_{0.5}Ni_{0.5}Fe_2O_4$, $Ag@Co_{0.5}Ni_{0.5}Fe_2O_4$, $Co_{0.5}Ni_{0.5}Fe_2O_4/GO$, and $Ag@Co_{0.5}Ni_{0.5}Fe_2O_4/GO$ nanocomposites was evaluated at room temperature within an applied magnetic field ranging from −20 000 to 20 000 Oersted (Oe). The M–H curves, depicted in Fig. 12, exhibit the characteristic ferrimagnetic behavior typically associated with spinel ferrites. The magnetic properties of $Co_{0.5}Ni_{0.5}Fe_2O_4$ and its modified composites were analyzed to understand the impact of Ag incorporation and GO incorporation on saturation magnetization ($M_s$), remanent magnetization ($M_r$), and coercivity ($H_c$), are summarized in Table 6. The pristine $Co_{0.5}Ni_{0.5}Fe_2O_4$ sample exhibited a coercivity of 517.17 Oe and a saturation magnetization ($M_s$) of 69.39 emu $g^{-1}$, indicating strong superexchange interactions among $Fe^{3+}$, $Co^{2+}$, and $Ni^{2+}$ ions. The relatively high remanence-to-saturation ratio (0.42) suggests a well-defined single-domain or pseudo-single-domain structure, which is commonly observed in spinel ferrites with high magneto-crystalline anisotropy.[80–82]

However, upon Ag incorporation ($Ag@Co_{0.5}Ni_{0.5}Fe_2O_4$), coercivity decreased to 488.32 Oe, and $M_s$ exhibited a substantial reduction to 23.07 emu $g^{-1}$. This significant drop in magnetization can be attributed to the substitution of non-magnetic Ag ions into the ferrite matrix, which dilutes the superexchange interaction and disrupts the $Fe^{3+}$–$O^{2-}$–$Fe^{3+}$ coupling, leading to a more magnetically soft behavior. Studies have reported that Ag incorporation in $CoFe_2O_4$ leads to decreased coercivity and $M_s$ due to structural distortion and reduced anisotropy energy. Additionally, the anisotropy constant decreased significantly from 13 957.5 erg $cm^{-3}$ to 1580.8 erg $cm^{-3}$, confirming the weakening of magneto crystalline anisotropy, which is consistent with earlier findings on Ag-doped spinel ferrites.[80,83,84]

In contrast, the incorporation of graphene oxide (GO) into the $Co_{0.5}Ni_{0.5}Fe_2O_4$ matrix ($Co_{0.5}Ni_{0.5}Fe_2O_4/GO$) resulted in a notable increase in coercivity to 820.93 Oe, while $M_s$ only slightly decreased to 60.64 emu $g^{-1}$. The increase in coercivity is attributed to strong interfacial interactions between GO sheets and ferrite nanoparticles, which introduce additional pinning effects and strain-induced anisotropy, impeding domain wall motion.[78–80] This phenomenon aligns with previous studies, where GO incorporation in ferrite nanocomposites resulted in enhanced coercivity due to increased anisotropy and interfacial strain effects. Furthermore, the anisotropy constant increased substantially to 18 396.7 erg $cm^{-3}$, supporting the claim that GO incorporation enhances structural anisotropy. Interestingly, remanence magnetization exhibited a slight increase (30.12 emu $g^{-1}$), indicating improved uniaxial anisotropy. However, when Ag-incorporation ferrite was further modified with GO ($Ag@Co_{0.5}Ni_{0.5}Fe_2O_4/GO$), coercivity drastically decreased to 207.63 Oe, and $M_s$ further dropped to 19.55 emu $g^{-1}$. The sharp decline in coercivity suggests that GO, in combination with Ag, introduces additional disorder, weakening exchange coupling and promoting multi-domain formation, which is often observed in hybrid systems with reduced magnetic anisotropy.[78,79,85] The reduction in $M_s$ is consistent with reports that Ag and GO, when co-integrated into ferrite matrices, lead to dilution of the magnetic phase and increased lattice defects, thereby decreasing overall magnetization. The significant drop in anisotropy constant (658.8 erg $cm^{-3}$) further supports the

Table 3 Parameters from Rietveld refinement and figures of merit for $Co_{0.5}Ni_{0.5}Fe_2O_4$, $Ag@Co_{0.5}Ni_{0.5}Fe_2O_4$, $Co_{0.5}Ni_{0.5}Fe_2O_4/GO$ and $Ag@Co_{0.5}Ni_{0.5}Fe_2O_4/GO$

| | | | | | Lattice parameter | | |
|---|---|---|---|---|---|---|---|
| Sample no. | $R_{exp}$ (%) | $R_{wp}$ (%) | RF (%) | GoF | $a$ (Å) | $V$ (Å$^3$) | X-ray density ($\rho_X$) (g $cm^{-3}$) |
| $Co_{0.5}Ni_{0.5}Fe_2O_4$ | 1.05 | 6.26 | 4.95 | 5.98 | 8.3540 | 583.01 | 5.362 |
| $Ag@Co_{0.5}Ni_{0.5}Fe_2O_4$ | 1.51 | 9.13 | 7.21 | 6.03 | 8.3757 | 587.57 | 5.507 |
| $Co_{0.5}Ni_{0.5}Fe_2O_4/GO$ | 1.06 | 6.37 | 5.07 | 5.99 | 8.3806 | 588.607 | 5.389 |
| $Ag@Co_{0.5}Ni_{0.5}Fe_2O_4/GO$ | 1.451 | 9.31 | 6.99 | 6.04 | 8.3347 | 578.98 | 5.383 |

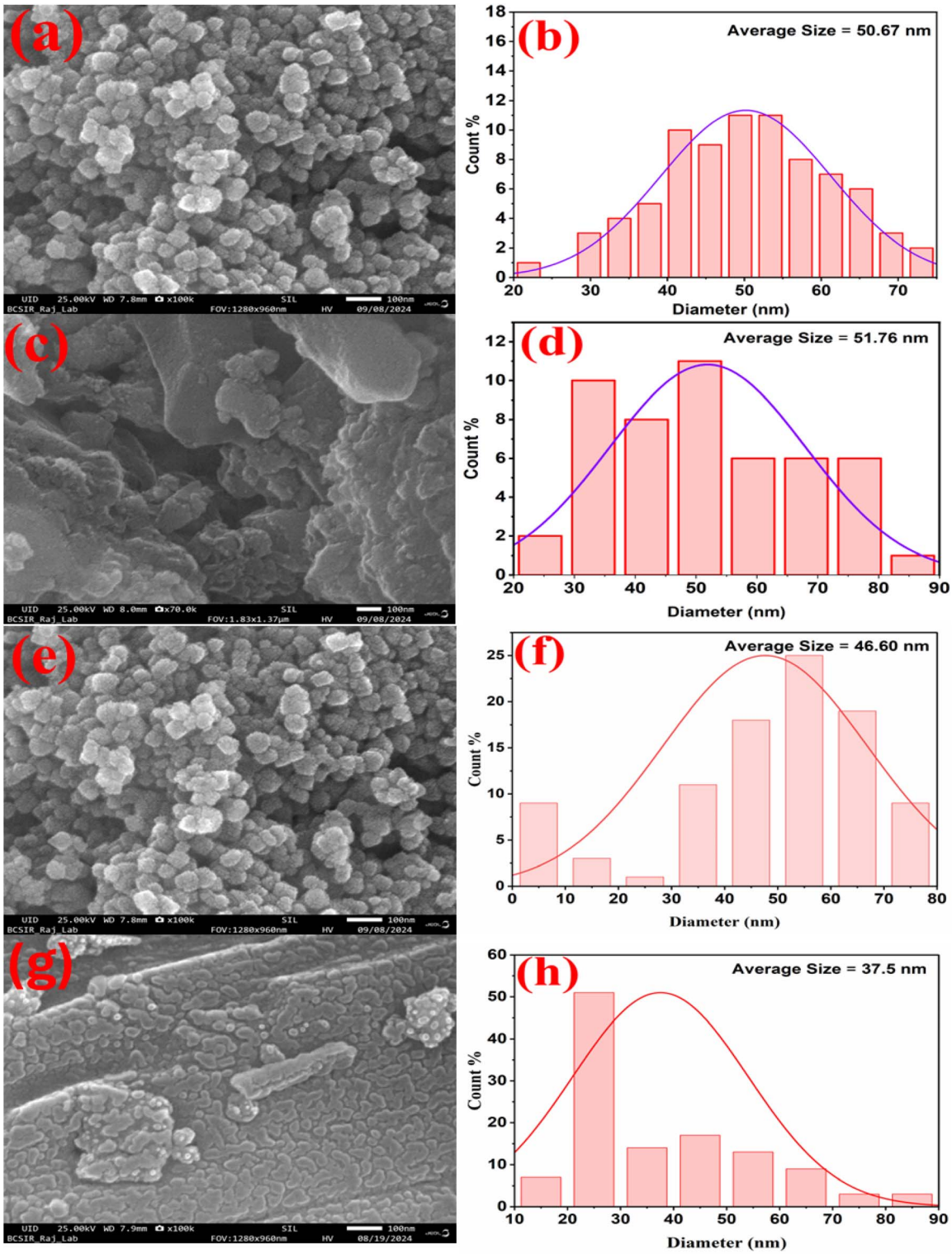


Fig. 10 FE-SEM images and particle size histogram of (a and b) $Co_{0.5}Ni_{0.5}Fe_2O_4$, (c and d) Ag@$Co_{0.5}Ni_{0.5}Fe_2O_4$, (e and f) $Co_{0.5}Ni_{0.5}Fe_2O_4$/GO and (g and h) Ag@$Co_{0.5}Ni_{0.5}Fe_2O_4$/GO.

hypothesis that the combined effect of Ag incorporation and GO incorporation results in a highly magnetically soft material, suitable for applications requiring low-coercivity nanocomposites.

These findings highlight the contrasting roles of Ag and GO in tuning the magnetic properties of ferrite nanocomposites. While Ag incorporation reduces coercivity and saturation magnetization by introducing non-magnetic ions that disrupt

Table 4 FE-SEM particle size analysis of $Co_{0.5}Ni_{0.5}Fe_2O_4$ and modified nanocomposites

| Sample | Diameter (nm) |
|---|---|
| $Co_{0.5}Ni_{0.5}Fe_2O_4$ | 50.57 |
| $Ag@Co_{0.5}Ni_{0.5}Fe_2O_4$ | 51.76 |
| $Co_{0.5}Ni_{0.5}Fe_2O_4$/GO | 46.60 |
| $Ag@Co_{0.5}Ni_{0.5}Fe_2O_4$/GO | 37.50 |

magnetic interactions, GO enhances coercivity and anisotropy in pure ferrite by strengthening interfacial pinning effects. However, the combination of Ag and GO suppresses anisotropy and exchange coupling, making the material more magnetically soft. The observed trends provide crucial insights into designing magnetically tunable nanomaterials for applications in high-frequency electronics, magnetic storage, and electromagnetic interference shielding. The study of $Ag@Co_{0.5}Ni_{0.5}Fe_2O_4$/GO suggests potential for low-coercivity, high-performance ferrite composites, particularly in biomedical applications such as targeted drug delivery and magnetic resonance imaging, where soft magnetic behavior is advantageous.[77,80,84]

The observed enhancement in both remanent and saturation magnetization in specific samples can be attributed to the strategic distribution of metal cations between the octahedral and tetrahedral coordination sites within the spinel lattice structure. A critical parameter for evaluating magnetic domain configurations is the squareness ratio ($S$), defined as the ratio of remanent magnetization ($M_r$) to saturation magnetization ($M_s$). This ratio provides insights into the domain behavior of a material, ranging from 0 (characteristic of superparamagnetic systems) to 1 (indicative of a purely ferromagnetic state).[86] The calculated $S$ values, as outlined in Table 5, consistently remain below 0.5, suggesting that the samples predominantly exhibit a single-domain or pseudo-single-domain magnetic configuration. According to the Stoner–Wohlfarth (S–W) model, an $S$ value exceeding 0.5 signifies the presence of multi-domain structures, while an $S$ value below this threshold is typically associated with single-domain magnetic behavior.[87] The tunability of the magnetic characteristics of $Co_{0.5}Ni_{0.5}Fe_2O_4$ nanoparticles is strongly influenced by morphological variations and particle size, both of which significantly modulate magnetocrystalline anisotropy and exchange interactions.

Conversely, the decline in saturation magnetization ($M_s$) observed in GO-integrated nanocomposites can be attributed to a reduction in Fe 3d state spin polarization combined with the inherent non-magnetic nature of graphene sheets. The presence of GO increases the effective surface area of the composite material, consequently enhancing surface disorder and disrupting exchange interactions, which leads to a further reduction in $M_s$.[88] Moreover, an increase in surface area facilitates a transition toward superparamagnetic-like behavior, thereby diminishing the net magnetic moment ($\mu_B$) and further lowering saturation magnetization. The magnetic moment was computed using the following expression eqn (22):

$$\mu_B = M_w \times \frac{M_s}{5585} \quad (22)$$

where $M_w$ represents the molecular weight of the sample. The incorporation of Ag induces a progressive decline in magnetic moment ($\mu_B$), exhibiting a trend similar to that of saturation magnetization, as presented in Table 5.[89] Furthermore, the anisotropy constant ($K$), a fundamental parameter governing the stability of magnetic moments, was determined using the relation (23):

$$K = (M_s \times H_c)/0.96 \quad (23)$$

The $K$ values, as summarized in Table 5, reveal a decreasing tendency with increasing graphene oxide (GO) concentration in the $Co_{0.5}Ni_{0.5}Fe_2O_4$/GO nanocomposites.[60] This trend signifies that GO effectively diminishes magnetocrystalline anisotropy, leading to a transition toward a more magnetically soft state. Such tunability in magnetic behavior holds significant implications for applications in high-frequency electronic devices, spintronic systems, and biomedical imaging technologies, where controlled magnetic responses are crucial for optimized performance.

### 3.4 Optical properties analysis

Diffuse-reflectance spectra were transformed *via* the Kubelka–Munk function $F(R) = (1 - R_\infty)^2/(2R_\infty)$. Under the assumptions of an ideal, infinitely thick, randomly scattering layer and weak absorption, $F(R)$ is proportional to the absorption coefficient $\alpha$. The Tauc relation $(F(R)h\nu)^2 = A(h\nu - E_g)$ for indirect transitions was therefore employed to estimate $E_g$ for all samples.

The UV-DRS analysis of the mixed ferrite and their composite nanorods, illustrated in Fig. 13a, shows significant absorption across the 200–800 nm wavelength range, with a notable absorption edge identified at 418 nm. The optical band gap energy ($E_g$) of these materials was calculated using the

Table 5 Elemental composition determined by EDX for $Co_{0.5}Ni_{0.5}Fe_2O_4$, $Ag@Co_{0.5}Ni_{0.5}Fe_2O_4$, $Co_{0.5}Ni_{0.5}Fe_2O_4$/GO and $Ag@Co_{0.5}Ni_{0.5}Fe_2O_4$/GO

| | Atom (%) | | | | | | |
|---|---|---|---|---|---|---|---|
| Sample name | C | O | Fe | Co | Ni | Ag | Ratio Co : Ni : Fe : Ag |
| $Co_{0.5}Ni_{0.5}Fe_2O_4$ | 0 | 25.58 | 48.22 | 13.83 | 12.37 | 0 | 0.56 : 0.5 : 1.95 : 0 |
| $Ag@Co_{0.5}Ni_{0.5}Fe_2O_4$ | 0 | 39.68 | 36.05 | 5.59 | 7.03 | 11.66 | 0.40 : 0.5 : 2.57 : 0.83 |
| $Co_{0.5}Ni_{0.5}Fe_2O_4$/GO | 13.07 | 26.70 | 38.70 | 11.13 | 10.40 | 0 | 0.54 : 0.5 : 1.86 : 0 |
| $Ag@Co_{0.5}Ni_{0.5}Fe_2O_4$/GO | 12.33 | 35.77 | 26.70 | 5.18 | 6.13 | 14.11 | 0.43 : 0.5 : 2.18 : 1.15 |

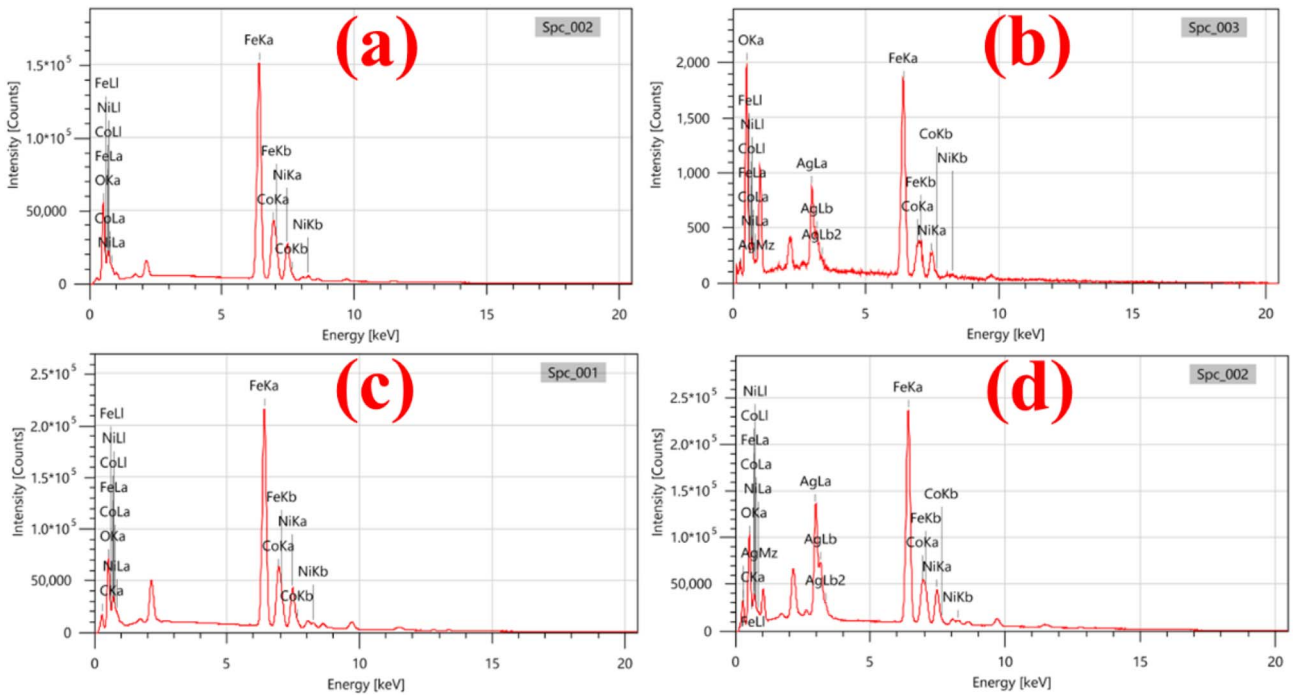


Fig. 11 EDX spectra of (a) $Co_{0.5}Ni_{0.5}Fe_2O_4$, (b) $Ag@Co_{0.5}Ni_{0.5}Fe_2O_4$, (c) $Co_{0.5}Ni_{0.5}Fe_2O_4$/GO and (d) $Ag@Co_{0.5}Ni_{0.5}Fe_2O_4$/GO.

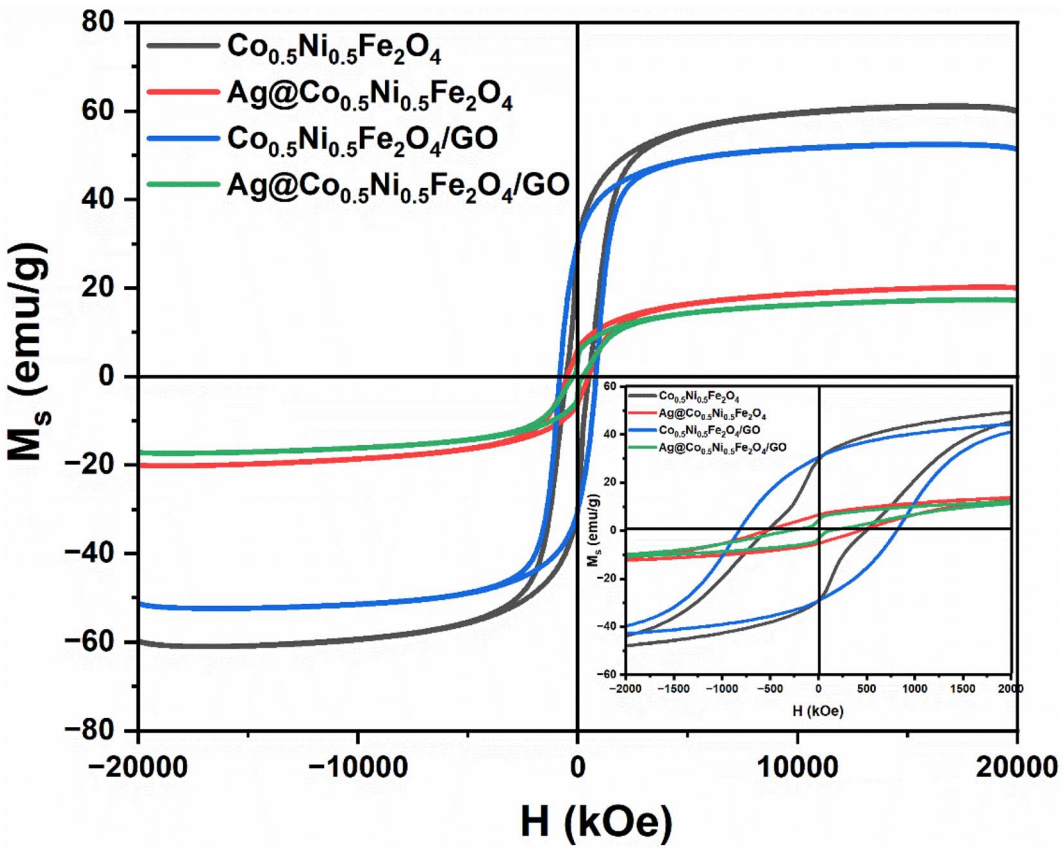


Fig. 12 Room temperature magnetization curves of $Co_{0.5}Ni_{0.5}Fe_2O_4$, $Ag@Co_{0.5}Ni_{0.5}Fe_2O_4$, $Co_{0.5}Ni_{0.5}Fe_2O_4$/GO and $Ag@Co_{0.5}Ni_{0.5}Fe_2O_4$/GO nanocomposite.

Table 6 The magnetic parameters like coercivity, remanent, saturation magnetization squareness ratio, magnetic moment and anisotropy constant

| Sample | Saturation mass magnetization (emu $g^{-1}$) | Coercivity (Oe) | Remanent mass magnetization (emu $g^{-1}$) | Squareness ratio | Magnetic moment ($\mu_B$) | Anisotropy constant |
|---|---|---|---|---|---|---|
| $Co_{0.5}Ni_{0.5}Fe_2O_4$ | 69.39 | 517.17 | 29.63 | 0.42 | 2.914 | 13 957.5 |
| $Ag@Co_{0.5}Ni_{0.5}Fe_2O_4$ | 23.07 | 488.32 | 6.06 | 0.26 | 0.969 | 1580.8 |
| $Co_{0.5}Ni_{0.5}Fe_2O_4/GO$ | 60.64 | 820.93 | 30.12 | 0.49 | 2.546 | 18 396.7 |
| $Ag@Co_{0.5}Ni_{0.5}Fe_2O_4/GO$ | 19.55 | 207.63 | 3.86 | 0.19 | 0.821 | 658.8 |

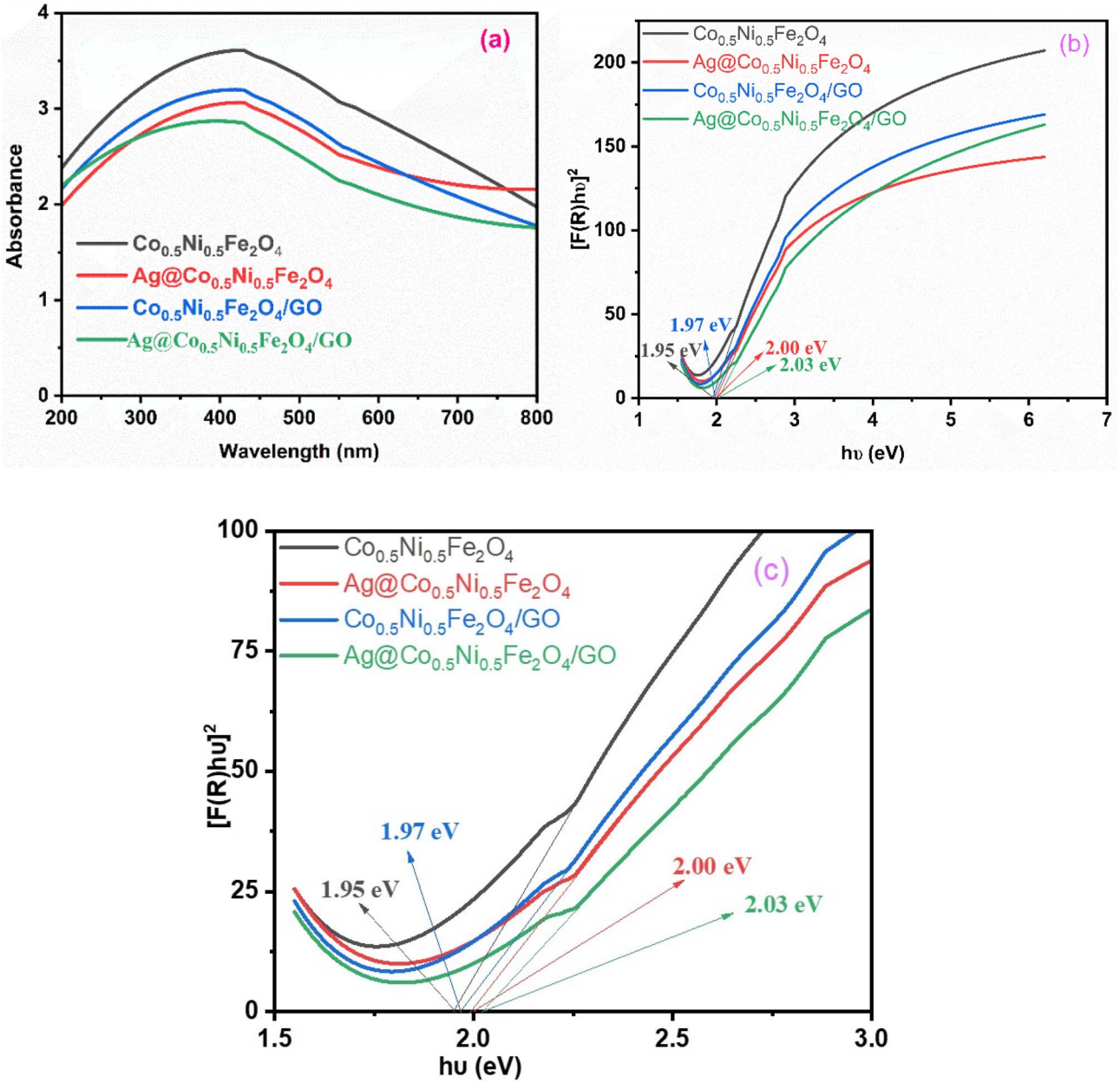


Fig. 13 Diagrams of (a) the UV-vis absorbance spectrum (b) $[F(R)h\nu]^2$ *versus* photoenergy and (c) narrow scale plot of $[F(R)h\nu]^2$ *versus* photoenergy for the produced nanocomposites.

Tauc method.[90] For the pure mixed ferrite, the $E_g$ was determined to be 1.95 eV (Fig. 13b). In contrast, the $E_g$ values for the $Co_{0.5}Ni_{0.5}Fe_2O_4/GO$, $Ag@Co_{0.5}Ni_{0.5}Fe_2O_4$, and $Ag@Co_{0.5}Ni_{0.5}Fe_2O_4/GO$ composites exhibited slight increases to 1.97 eV, 2.00 eV, and 2.03 eV, respectively. The narrower scale plot of $[F(R)h\nu]^2$ *versus* photoenergy has been shown in Fig. 13c

 

to make the band gap clear and understandable. This increment is likely due to a decrease in visible light absorption within the composites, as evidenced by the absorption spectra.

The slight blue-shift (1.95 → 2.03 eV) is attributed to quantum-size confinement and the tensile strain introduced by the Ag|ferrite and GO|ferrite interfaces. Although a wider band-gap narrows visible-light absorption, three cooperative effects override this drawback: (i) surface-plasmon resonance (SPR) of Ag injects hot electrons into the CB of the ferrite, (ii) GO acts as an ultrafast electron highway suppressing $e^-/h^+$ recombination, and (iii) the higher CB potential (after upshifting) favours $^{\bullet}O_2^-$ radical generation. Together these factors yield net higher MB-degradation efficiency despite the bandgap widening. The combination of a low band gap and nanoscale particle dimensions significantly enhances the photocatalytic performance of the nanorods when subjected to solar irradiation.[90] It is postulated that the photocatalytic activity benefits from robust absorption over a wide spectral range, which spans both UV and visible light.[91] The observed red shift in the absorption band broadens the photoexcitation spectrum, enabling the photocatalyst to absorb a greater number of incident photons, thereby improving its overall photocatalytic efficiency.

### 3.5 Dielectric properties analysis

Fig. 14a illustrates the fluctuation in the dielectric constant of the materials across an extensive frequency range, spanning from 20 Hz to 20 MHz. The observed data indicates a significant reduction in the dielectric constant reaching up to 1 kHz, followed by a more gradual decline as the frequency increases.

At approximately 10 kHz, the dielectric constant stabilizes, indicating the onset of dielectric dispersion. The relatively high dielectric constant observed at lower frequencies can be attributed to heterogeneous conduction present in the composite materials. The overall decrease in dielectric constant with increasing frequency implies that the polarization behavior of the ferrite is intricately linked to the conduction pathways, which are influenced by the localized motion of

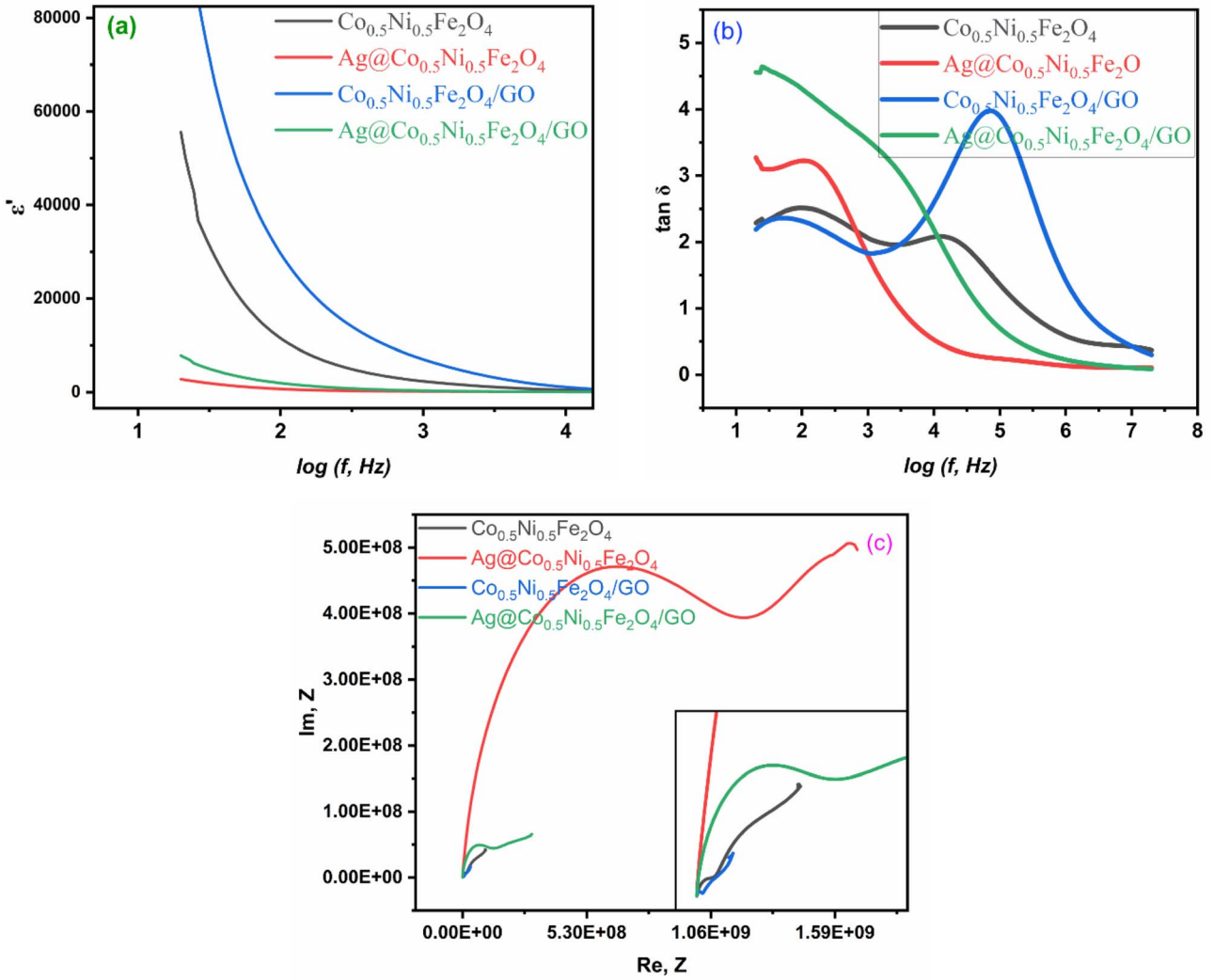


Fig. 14 (a) Dielectric constant ($\varepsilon'$) as a function of frequency (log $f$), (b) dielectric loss tangent (tan $\delta$) as a function of frequency (log $f$), (c) the Nyquist plots obtained for $Co_{0.5}Ni_{0.5}Fe_2O_4$, $Ag@Co_{0.5}Ni_{0.5}Fe_2O_4$, $Co_{0.5}Ni_{0.5}Fe_2O_4$/GO and $Ag@Co_{0.5}Ni_{0.5}Fe_2O_4$/GO.

electrons in the presence of an electric field. This movement is further facilitated by the electron exchange between $Fe^{2+}$ and $Fe^{3+}$ ions.[92]

This movement governs the polarization behavior of ferrite material. Polarization is well-established as diminishes the intensity of the electric field within the medium. The reduction in polarization as frequency increases may stem from the inability of electronic interactions between $Fe^{2+}$ and $Fe^{3+}$ ions to keep up with the alternating electric field at higher frequencies.[93] Consequently, the dielectric constantly experiences a notable decrease with the rise in frequency. This dispersion phenomenon aligns with the Maxwell–Wagner model of interfacial polarization and can be interpreted through Koop's phenomenological theory.[58,94,95] The presence of free charge carriers within the material plays a significant role in this behavior. As the frequency increases, the contribution of polarization from space charges diminishes because these free charge carriers are unable to respond swiftly enough to the changing electric field. As a result, only dipolar polarization remains significant, which accounts for the stable value of the real component of the dielectric properties observed in the frequency range of 10 kHz to 20 MHz.[96] The addition of graphene oxide (GO) results in an enhanced dielectric constant, likely due to its superior conductivity, as well as the improved polarization and conductivity within the nanocomposites, which collectively enhance their overall dielectric characteristics.[97,98] The observed decline in the dielectric constant of the ferrite with the incorporation of silver (Ag) nanoparticles can be attributed to the interference these nanoparticles introduce into the polarization of the ferrites. This disruption in polarization ultimately leads to a reduction in the dielectric constant values.[99] Incorporation of highly conductive Ag nanoparticles forms interfacial space-charge regions that partially screen the local electric field inside ferrite grains. This screening reduces dipole density—and hence $\varepsilon'$—by hindering $Fe^{2+} \leftrightarrow Fe^{3+}$ hopping polarisation, explaining the observed drop in dielectric constant upon Ag addition.

Fig. 14b shows the frequency-dependent behavior of the dissipation factor, also known as the dielectric loss tangent (tan $\delta$), for the materials under study. The behavior of tan $\delta$ closely parallels that of the dielectric constant, exhibiting a decline as frequency increases, which is attributed to diminished polarization under higher alternating current (AC) fields. At elevated frequencies, particularly near 8 kHz, the values of tan $\delta$ reach a plateau. This frequency-dependent variation in tan $\delta$ is associated with the conduction mechanisms in ferrites and aligns with Koop's empirical model.[100,101] The curve for the loss factor is believed to be affected by domain wall resonance. According to Rezlescu's model, when the movement of domain walls is constrained, losses are minimized at higher frequencies. A minor irregularity was noted at lower frequencies, which, per Rezlescu's model, could result from the distinct impacts of both positive (p) and negative (n) charge carriers on the relaxation peak. This behavior is further influenced by the electrical interactions between $Fe^{2+}$ and $Fe^{3+}$ ions. Moreover, the dielectric loss tangent is intricately linked to conductance; higher conductance values typically lead to increased dielectric losses.[71,102] It is also acknowledged that dielectric loss can stem from factors such as grain boundaries, impurities, and defects present within the crystal lattice. This phenomenon occurs as polarization trails behind the applied alternating electric field, resulting in energy dissipation within the material.[58,93]

Fig. 14c displays Nyquist impedance plots for $Co_{0.5}Ni_{0.5}Fe_2O_4$, $Ag@Co_{0.5}Ni_{0.5}Fe_2O_4$, $Co_{0.5}Ni_{0.5}Fe_2O_4$/GO, and $Ag@Co_{0.5}Ni_{0.5}Fe_2O_4$/GO, illustrating how the inherent low conductivity of ferrites influences the behavior of grain boundaries. This limitation in conductivity hampers the movement of $Fe^{2+}$ and $Fe^{3+}$ ions at lower frequencies. However, with increasing frequency of the applied electric field, the conductive grains respond more actively, promoting ion mobility. Gaining insight into this conduction mechanism is essential for identifying its primary source, whether it arises from the grains, the grain boundaries, or stray charges present within the electrode. Impedance spectroscopy is an essential method for distinguishing the individual roles of bulk (grain) and grain boundary components in the material's total conductivity. The plots exhibit a single semicircular arc in the high-to-medium frequency range, accompanied by a slanted line in the low-frequency domain. The semicircular arc is indicative of charge transfer resistance ($R_{ct}$).[103] Notably, in the impedance spectra of the ferrite materials, a pattern emerges in which the diameters of the semicircles diminish with the incorporation of graphene oxide (GO). This reduction in diameter suggests an enhancement in conductivity due to the addition of these materials, which aligns with our previous findings. The semicircle's diameter reflects the resistance to interfacial charge transfer, where a smaller diameter indicates faster charge transfer and reduced charge recombination. Such improvements in charge dynamics significantly bolster catalytic activity.[104,105]

### 3.6 Photocatalytic activity

The photocatalytic performance of the synthesized samples – $Co_{0.5}Ni_{0.5}Fe_2O_4$, $Ag@Co_{0.5}Ni_{0.5}Fe_2O_4$, $Co_{0.5}Ni_{0.5}Fe_2O_4$/GO, and $Ag@Co_{0.5}Ni_{0.5}Fe_2O_4$/GO – was assessed for their ability to degradation of methylene blue (MB) dye under visible light exposure. The absorption spectra of the dye solution, as shown in Fig. 15a–d, were recorded at various time intervals while employing these different catalysts. A significant reduction in the intensity of the MB absorption peak at 660 nm was noted as the exposure time increased, with the peak eventually vanishing after 180 minutes of irradiation. In contrast, the blank sample, which did not contain any catalyst, exhibited only minimal self-decomposition of the MB dye when subjected to visible light. The sequence of photocatalytic efficiency for the tested materials was: $Ag@Co_{0.5}Ni_{0.5}Fe_2O_4$/GO > $Co_{0.5}Ni_{0.5}Fe_2O_4$/GO > $Ag@Co_{0.5}Ni_{0.5}Fe_2O_4$ > $Co_{0.5}Ni_{0.5}Fe_2O_4$. After 180 minutes of light exposure, the intensity of the absorption peak at 660 nm nearly vanished for all samples, with degradation efficiencies of 55.57%, 67.02%, 70.94%, and 96.59%, respectively, as shown in Fig. 15e. The significant improvement in photocatalytic efficiency for $Co_{0.5}Ni_{0.5}Fe_2O_4$/GO is attributed to the incorporation of graphene oxide (GO) into the nanocomposite, enhancing electron–hole pair separation due to the high electron transfer

 

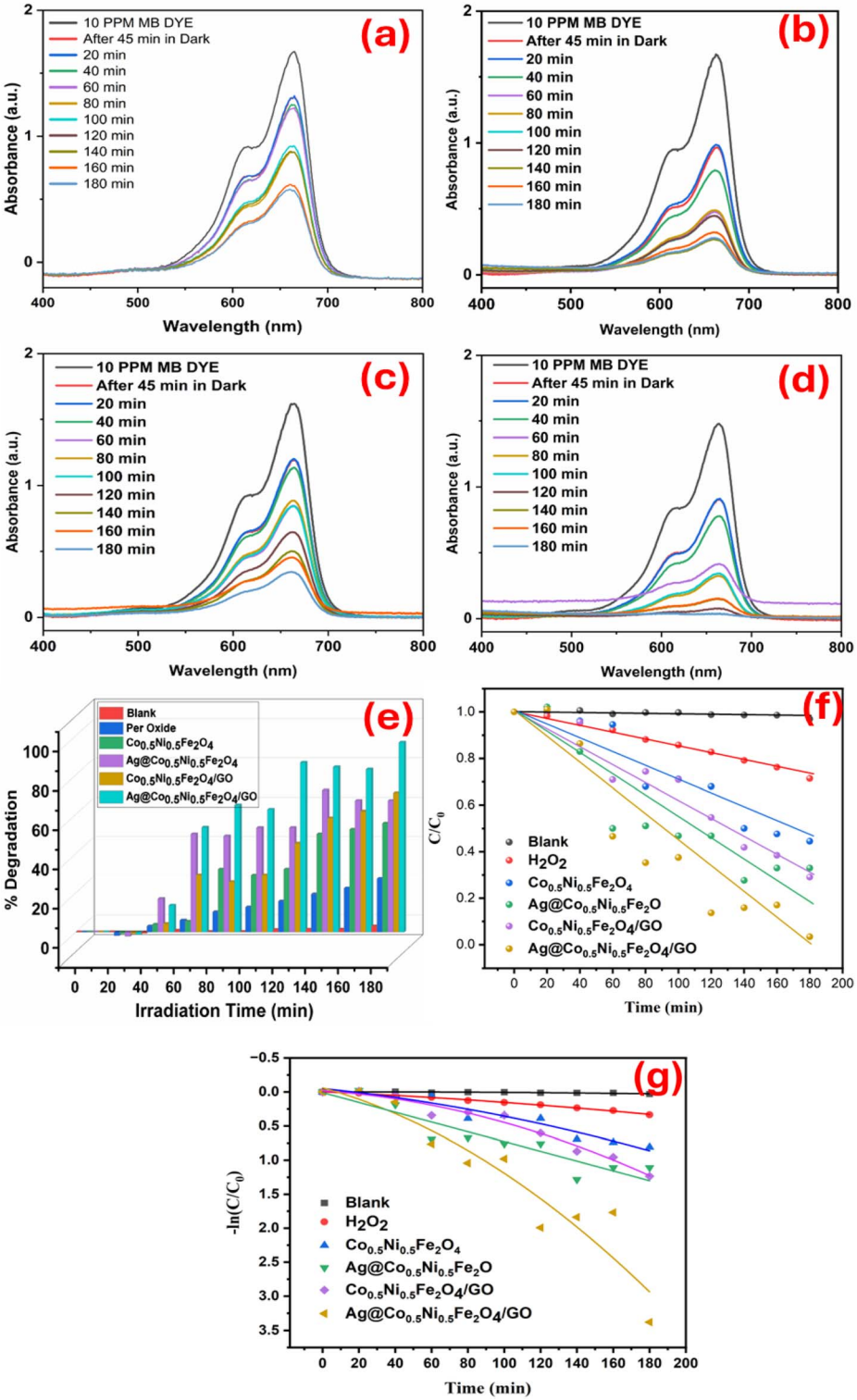


Fig. 15 Spectral absorption during the photocatalytic degradation of MB by (a) $Co_{0.5}Ni_{0.5}Fe_2O_4$, (b) $Ag@Co_{0.5}Ni_{0.5}Fe_2O_4$, (c) $Co_{0.5}Ni_{0.5}Fe_2O_4$/GO, (d) $Ag@Co_{0.5}Ni_{0.5}Fe_2O_4$/GO, (e) % degradation for corresponding samples, (f) changes in ($C/C_0$) with respect to irradiation time, and (g) the first-order kinetics fitting for MB degradation.

capability of the $Co_{0.5}Ni_{0.5}Fe_2O_4$ nanoparticles.[106] Furthermore, the incorporation of graphene into $Co_{0.5}Ni_{0.5}Fe_2O_4$/GO and $Ag@Co_{0.5}Ni_{0.5}Fe_2O_4$/GO significantly improves the efficiency of electron–hole pair separation, which contributes to the enhanced photocatalytic performance observed in $Ag@Co_{0.5}Ni_{0.5}Fe_2O_4$/GO.[88] This improved activity can be credited to the SPR (surface plasmon resonance) effect exhibited by the silver nanoparticles (Ag NPs). This phenomenon not only enhances

the catalytic activity but also facilitates the formation of additional active sites through the deposition of plasmonic metals onto $Co_{0.5}Ni_{0.5}Fe_2O_4$.[107]

Fig. 15f illustrate that the degradation process adheres to a pseudo-first-order reaction mechanism, with the reaction rate constants ($k$) determined for each of the synthesized samples. Among them, the Ag@$Co_{0.5}Ni_{0.5}Fe_2O_4$/GO composite demonstrated the most significant reaction rate, with a constant of $k = 0.01665\ min^{-1}$. In comparison, the $Co_{0.5}Ni_{0.5}Fe_2O_4$/GO sample showed a slightly lower rate of $k = 0.00717\ min^{-1}$, while the Ag@$Co_{0.5}Ni_{0.5}Fe_2O_4$ yielded a rate of $k = 0.00692\ min^{-1}$, and the $Co_{0.5}Ni_{0.5}Fe_2O_4$ sample presented an equivalent rate of $k = 0.00507\ min^{-1}$ when subjected to halogen light irradiation.[58] The proposed degradation mechanisms are shown in Fig. 16.

The synthesized Ag@$Co_{0.5}Ni_{0.5}Fe_2O_4$/GO nanocomposite exhibited the highest photocatalytic efficiency, achieving 96.59% degradation of methylene blue under visible light irradiation, surpassing the efficiencies reported in other studies, as shown in Table 7. This superior performance is attributed to the synergistic effects of silver's surface plasmon resonance (SPR) and the enhanced electron transfer capabilities of graphene oxide. The $Co_{0.5}Ni_{0.5}Fe_2O_4$/GO composite also exhibited significant improvement over the pristine $Co_{0.5}Ni_{0.5}Fe_2O_4$, reinforcing the role of graphene oxide in suppressing electron–hole recombination. Compared to other reported ferrite-based nanocomposites, the Ag@$Co_{0.5}Ni_{0.5}Fe_2O_4$/GO nanocomposite outperforms similar systems, such as $MgFe_2O_4$ and $NiFe_2O_4$/g-$C_3N_4$, which showed slightly lower degradation efficiencies within shorter reaction times.[108]

Photocatalytic charge-transfer cascade has shown in Fig. 16a and b. Under visible irradiation the localised surface-plasmon resonance (LSPR) of Ag nanoparticles produces hot electrons with energies up to ≈2 eV above the Ag Fermi level ($E_F \approx 4.26$ eV). These electrons surmount the 0.35 eV Schottky barrier and inject into the conduction band (CB) of $Co_{0.5}Ni_{0.5}Fe_2O_4$ ($E_{CB} \approx -0.65$ V *vs.* NHE). Simultaneously, graphene oxide (GO, work function 4.7 eV) acts as an ultrafast electron "highway", extracting CB electrons within a few picoseconds and shuttling them to dissolved $O_2$. The resulting space-charge layer at the Ag|ferrite interface traps photogenerated holes in the valence band (VB), suppressing $e^-/h^+$ recombination even though the dark charge-transfer resistance (Nyquist semicircle) is marginally higher for the Ag-decorated sample.

Reactive-oxygen-species (ROS) formation and pollutant degradation (Fig. 16c). CB electrons reduce $O_2$ to super-oxide radicals ($^{\bullet}O_2^-$, $E^{\circ} = -0.33$ V). Proton-coupled electron transfer yields $HO_2^{\bullet}/H_2O_2$, which further decomposes to $^{\bullet}OH$ radicals.[113,114] Concurrently, VB holes ($E_{VB} \approx +1.55$ V) oxidise surface-adsorbed $H_2O$ (or $OH^-$) to $^{\bullet}OH$. These ROS attack the azo bond and aromatic rings of methyl-blue (MB), forming low-molecular intermediates that mineralise to $CO_2$, $NO_3^-$ and $SO_4^{2-}$. The dual pathway—plasmonic hot-electron injection plus GO-mediated charge shuttling—explains why Ag@$Co_{0.5}Ni_{0.5}Fe_2O_4$/GO outperforms the bare ferrite/GO composite despite its larger dark-state. Comparable mechanisms have been reported for Ag/$TiO_2$–RGO,[115] Ag-loaded ZnO–graphene hybrid nanocomposites[116] and Ag@$ZnFe_2O_4$/graphene.[117]

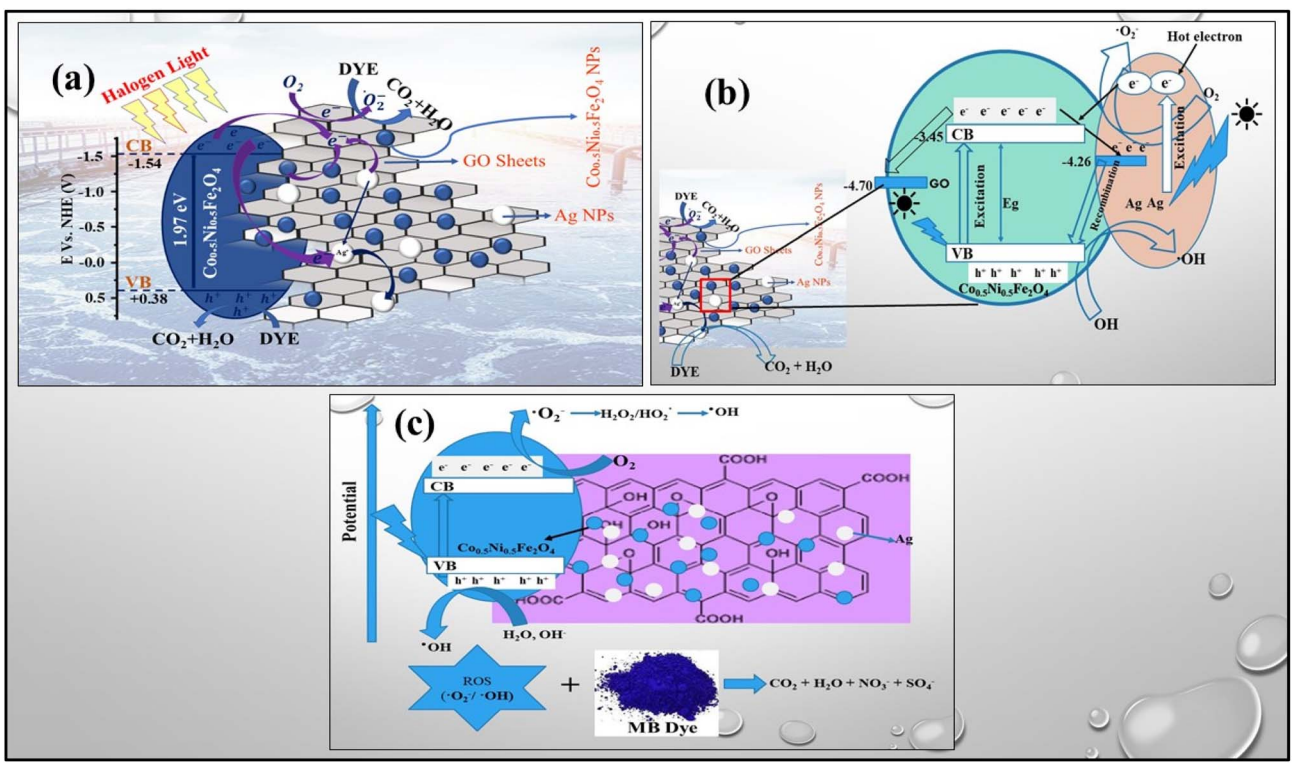


Fig. 16 Dye degradation mechanism on Ag@$Co_{0.5}Ni_{0.5}Fe_2O_4$/GO catalyst under halogen light irradiation. (a) Photocatalytic charge transfer cascade, (b) photocatalytic charge transfer case with LSPR effect of Ag, (c) reactive-oxygen-species (ROS) formation and pollutant degradation.

Table 7 Comparative study of photocatalytic performance

| Composites | Dye | Medium | Time | % degradation | Ref. |
|---|---|---|---|---|---|
| $MgFe_2O_4$, 30 mg | Methylene blue, 10 ppm | Visible light | 120 | 87.3 | 108 |
| $NiFe_2O_4$/g-$C_3N_4$, 20 mg | Congo red, 20 ppm | UV-vis | 90 | 92.5 | 108 |
| $CoFe_2O_4$/$TiO_2$, 15 mg | Methyl orange, 25 ppm | Solar light | 150 | 89.6 | 109 |
| $Mn_{0.6}Zn_{0.4}Fe_2O_4$/g-$C_3N_4$, 20 mg | Methylene blue, 20 ppm | Sunlight | 150 | 94.2 | 110 |
| $MgFe_2O_4$, 25 mg | Rhodamine B, 10 ppm | Visible light | 120 | 85.7 | 111 |
| SFGCN nanocomposite, 30 mg | Methyl orange, 15 ppm | Solar light | 180 | 91.4 | 112 |
| $Co_{0.5}Ni_{0.5}Fe_2O_4$/GO, 25 mg | Methylene blue, 10 ppm | Visible light | 180 | 70.94 | This work |
| Ag@$Co_{0.5}Ni_{0.5}Fe_2O_4$/GO, 25 mg | Methylene blue, 10 ppm | Visible light | 180 | 96.59 | This work |

## 4. Conclusion

$Co_{0.5}Ni_{0.5}Fe_2O_4$ nanoparticles and their composites with silver (Ag) and graphene oxide (GO) were successfully synthesized using a facile co-precipitation method. Structural analysis *via* X-ray diffraction confirmed the formation of cubic spinel ferrite structures with crystallite sizes ranging from 25.5 nm to 80.9 nm. Morphological characterization revealed uniformly distributed, spherical nanoparticles anchored on GO sheets, with an average particle size of 37.5 nm, as observed through FE-SEM imaging and confirmed by EDX spectroscopy.

Magnetic measurements indicated ferromagnetic behavior with systematic variations attributable to the incorporation of Ag and GO. Notably, the Ag@$Co_{0.5}Ni_{0.5}Fe_2O_4$/GO nanocomposite exhibited exceptional photocatalytic performance, achieving a 96.59% degradation efficiency of methylene blue under visible light irradiation. This enhanced activity is attributed to the synergistic effects of Ag's plasmonic properties and GO's conductive network, which collectively reduce the bandgap energy, facilitate efficient charge separation and transfer, and suppress electron–hole recombination. These findings advance the understanding of how integrating noble metals and graphene derivatives with magnetic nanoparticles can significantly enhance photocatalytic properties. This work paves the way for developing highly efficient and durable photocatalysts for wastewater treatment and broader environmental purification technologies. Future research could explore scaling up the synthesis method and evaluating the nanocomposite's effectiveness against a wider range of pollutants, potentially expanding its applicability in environmental technologies.

## Author contributions

Shahanaz Parvin: investigation, formal analysis, methodology, software, visualization, writing – original draft. Md. Lutfor Rahman: conceptualization, investigation, data curation, methodology, software, supervision, validation, project administration, visualization, writing – review & editing. Faisal Islam Chowdhury: supervision, writing – review & editing. Bristy Biswas: data curation, validation, visualization. Md. Farid Ahmed: data curation, validation, visualization. Moksodur Rahman: visualization, software, formal analysis. Md. Al-Amin: data curation. Md. Kamrul Hossain: supervision, writing – review & editing. Shirin Akter Jahan: resources, writing – review & editing. Nahid Sharmin: resources, funding acquisition, supervision, writing – review & editing.

## Conflicts of interest

The authors declare no conflict of interest.

## Data availability

Data will be available on request.

## Acknowledgements

The authors would like to acknowledge Institute of Glass and Ceramic Research & Testing (IGCRT), Bangladesh Council of Scientific and Industrial Research (BCSIR), Dhaka, Bangladesh for providing technical supports.

## References

1 M. V. Kovalenko, et al., Prospects of nanoscience with nanocrystals, *ACS Nano*, 2015, **9**(2), 1012–1057, DOI: 10.1021/nn506223h.
2 P. Baskaran and M. Rajasekar, Recent trends and future perspectives of thermoelectric materials and their applications, *RSC Adv.*, 2024, **14**, 21706–21744, DOI: 10.1039/d4ra03625e.
3 L. Hossain, S. K. Sarker and M. S. Khan, Evaluation of present and future wastewater impacts of textile dyeing industries in Bangladesh, *Environ. Dev.*, 2018, **26**, 23–33, DOI: 10.1016/j.envdev.2018.03.005.
4 K. Gomes, S. Caucci, J. Morris, E. Guenther and J. Miggelbrink, Sustainability transformation in the textile industry—The case of wastewater management, *Bus. Strategy Dev.*, 2024, 7(1), e324, DOI: 10.1002/bsd2.324.
5 S. Sarkar, A. Banerjee, U. Halder, R. Biswas and R. Bandopadhyay, Degradation of Synthetic Azo Dyes of Textile Industry: a Sustainable Approach Using Microbial Enzymes, *Water Conserv. Sci. Eng.*, 2017, **2**, 121–131, DOI: 10.1007/s41101-017-0031-5.
6 S. Khan and A. Malik, Environmental and health effects of textile industry wastewater, in *Environmental Deterioration and Human Health: Natural and Anthropogenic*

*Determinants*, Springer Netherlands, 2014, pp. 55–71, DOI: 10.1007/978-94-007-7890-0_4.

7 G. Samchetshabam, T. G. Choudhury and S. Gita, Impact of Textile Dyes Waste on Aquatic Environments and its Treatment, *Environ. Ecol.*, 2017, **35**, 2349–2353.

8 S. Nayak, G. Swain and K. Parida, Enhanced Photocatalytic Activities of RhB Degradation and $H_2$ Evolution from in Situ Formation of the Electrostatic Heterostructure $MoS_2$/NiFe LDH Nanocomposite through the Z-Scheme Mechanism via p-n Heterojunctions, *ACS Appl. Mater. Interfaces*, 2019, **11**(23), 20923–20942, DOI: 10.1021/acsami.9b06511.

9 S. Nayak, K. Kumar Das and K. Parida, Indulgent of the physiochemical features of MgCr-LDH nanosheets towards photodegradation process of methylene blue, *J. Colloid Interface Sci.*, 2023, **634**, 121–137, DOI: 10.1016/j.jcis.2022.12.050.

10 S. Peiris, H. B. de Silva, K. N. Ranasinghe, S. V. Bandara and I. R. Perera, Recent development and future prospects of $TiO_2$ photocatalysis, *J. Chin. Chem. Soc.*, 2021, **68**, 738–769, DOI: 10.1002/jccs.202000465.

11 K. Nakata and A. Fujishima, $TiO_2$ photocatalysis: Design and applications, *J. Photochem. Photobiol., C*, 2012, **13**(3), 169–189, DOI: 10.1016/j.jphotochemrev.2012.06.001.

12 Z. Mirzaeifard, Z. Shariatinia, M. Jourshabani and S. M. Rezaei Darvishi, ZnO Photocatalyst Revisited: Effective Photocatalytic Degradation of Emerging Contaminants Using S-Doped ZnO Nanoparticles under Visible Light Radiation, *Ind. Eng. Chem. Res.*, 2020, **59**(36), 15894–15911, DOI: 10.1021/acs.iecr.0c03192.

13 C. Sun, et al., Recent intensification strategies of $SnO_2$-based photocatalysts: A review, *Chem. Eng. J.*, 2022, **427**, 131564, DOI: 10.1016/j.cej.2021.131564.

14 R. Rameshbabu and B. Neppolian, Surfactant Assisted Hydrothermal Synthesis of Superparamagnetic $ZnFe_2O_4$ Nanoparticles as an Efficient Visible-Light Photocatalyst for the Degradation of Organic Pollutant, *J. Cluster Sci.*, 2016, **27**(6), 1977–1987, DOI: 10.1007/s10876-016-1057-0.

15 D. Chahar, et al., Photocatalytic activity of cobalt substituted zinc ferrite for the degradation of methylene blue dye under visible light irradiation, *J. Alloys Compd.*, 2021, **851**, 156878, DOI: 10.1016/j.jallcom.2020.156878.

16 A. Behera, D. Kandi, S. Mansingh, S. Martha and K. Parida, Facile synthesis of $ZnFe_2O_4$@RGO nanocomposites towards photocatalytic ciprofloxacin degradation and $H_2$ energy production, *J. Colloid Interface Sci.*, 2019, **556**, 667–679, DOI: 10.1016/j.jcis.2019.08.109.

17 S. H. U. Din, et al., Ag-doped nickel ferrites and their composite with rGO: Synthesis, characterization, and solar light induced degradation of coloured and colourless effluents, *Ceram. Int.*, 2022, **48**(11), 15629–15639, DOI: 10.1016/j.ceramint.2022.02.097.

18 Q. A. Pankhurst, N. K. T. Thanh, S. K. Jones and J. Dobson, Progress in applications of magnetic nanoparticles in biomedicine, *J. Phys. D: Appl. Phys.*, 2009, **42**(22), 224001, DOI: 10.1088/0022-3727/42/22/224001.

19 S. J. Salih and W. M. Mahmood, Review on magnetic spinel ferrite ($MFe_2O_4$) nanoparticles: From synthesis to application, *Heliyon*, 2023, **9**, e16601, DOI: 10.1016/j.heliyon.2023.e16601.

20 A. Soufi, et al., Recent trends in magnetic spinel ferrites and their composites as heterogeneous Fenton-like catalysts: A review, *J. Environ. Manage.*, 2024, **367**, 121971, DOI: 10.1016/j.jenvman.2024.121971.

21 V. Jeseentharani, M. George, B. Jeyaraj, A. Dayalan and K. S. Nagaraja, Synthesis of metal ferrite ($MFe_2O_4$, M = Co, Cu, Mg, Ni, Zn) nanoparticles as humidity sensor materials, *J. Exp. Nanosci.*, 2013, **8**(3), 358–370, DOI: 10.1080/17458080.2012.690893.

22 Rachna, N. B. Singh and A. Agarwal, Preparation, Characterization, Properties and Applications of Nano Zinc Ferrite, *Mater. Today: Proc.*, 2018, 9148–9155, DOI: 10.1016/j.matpr.2017.10.035.

23 M. V. Nikolic, et al., Investigation of $ZnFe_2O_4$ spinel ferrite nanocrystalline screen-printed thick films for application in humidity sensing, *Int. J. Appl. Ceram. Technol.*, 2019, **16**(3), 981–993, DOI: 10.1111/ijac.13190.

24 K. K. Das, et al., Enhanced photocatalytic activities of polypyrrole sensitized zinc ferrite/graphitic carbon nitride n-n heterojunction towards ciprofloxacin degradation, hydrogen evolution and antibacterial studies, *J. Colloid Interface Sci.*, 2020, **561**, 551–567, DOI: 10.1016/j.jcis.2019.11.030.

25 S. Patnaik, K. K. Das, A. Mohanty and K. Parida, Enhanced photo catalytic reduction of Cr(VI) over polymer-sensitized g-$C_3N_4$/$ZnFe_2O_4$ and its synergism with phenol oxidation under visible light irradiation, *Catal. Today*, 2018, **315**, 52–66, DOI: 10.1016/j.cattod.2018.04.008.

26 K. K. Das, L. Paramanik and K. Parida, An insight to band-bending mechanism of polypyrrole sensitized B-rGO/$ZnFe_2O_4$ p-n heterostructure with dynamic charge transfer for photocatalytic applications, *Int. J. Hydrogen Energy*, 2021, **46**(48), 24484–24500, DOI: 10.1016/j.ijhydene.2021.05.019.

27 M. Chandrika, A. V. Ravindra, C. Rajesh, S. D. Ramarao and S. Ju, Studies on structural and optical properties of nano $ZnFe_2O_4$ and $ZnFe_2O_4$-$TiO_2$ composite synthesized by co-precipitation route, *Mater. Chem. Phys.*, 2019, **230**, 107–113, DOI: 10.1016/j.matchemphys.2019.03.059.

28 K. K. Das, S. Mansingh, D. P. Sahoo, R. Mohanty and K. Parida, Engineering an oxygen-vacancy-mediated step-scheme charge carrier dynamic coupling $WO_{3-x}$/$ZnFe_2O_4$ heterojunction for robust photo-Fenton-driven levofloxacin detoxification, *New J. Chem.*, 2022, **46**(12), 5785–5798, DOI: 10.1039/d2nj00067a.

29 Y. Xu, Y. Liang, L. Jiang, H. Wu, H. Zhao and D. Xue, Preparation and magnetic properties of $ZnFe_2O_4$ nanotubes, *J. Nanomater.*, 2011, **2011**, 12274–12278, DOI: 10.1155/2011/525967.

30 M. Bohra, V. Alman and R. Arras, Nanostructured $ZnFe_2O_4$: An exotic energy material, *Nanomaterials*, 2021, **11**(5), 1286, DOI: 10.3390/nano11051286.

31 J. A. Gomes, et al., $ZnFe_2O_4$ nanoparticles for ferrofluids: A combined XANES and XRD study, *J. Magn. Magn. Mater.*,

2011, **323**(10), 1203–1206, DOI: **10.1016/j.jmmm.2010.11.006**.

32 K. Wu, J. Li and C. Zhang, Zinc ferrite based gas sensors: A review, *Ceram. Int.*, 2019, **45**(9), 11143–11157, DOI: **10.1016/j.ceramint.2019.03.086**.

33 J. Zhang, et al., Preparation of core/shell-structured $ZnFe_2O_4$@$ZnIn_2S_4$ catalysts and its ultrafast microwave catalytic reduction performance for aqueous Cr(VI), *Chem. Eng. J.*, 2023, **451**(P1), 138182, DOI: **10.1016/j.cej.2022.138182**.

34 Y. Fu, X. Sun and X. Wanga, $BiVO_4$-graphene catalyst and its high photocatalytic performance under visible light irradiation, *Mater. Chem. Phys.*, 2011, **131**(1–2), 325–330, DOI: **10.1016/j.matchemphys.2011.09.049**.

35 S. P. Meshram, P. V. Adhyapak, U. P. Mulik and D. P. Amalnerkar, Facile synthesis of CuO nanomorphs and their morphology dependent sunlight driven photocatalytic properties, *Chem. Eng. J.*, 2012, **204–205**, 158–168, DOI: **10.1016/j.cej.2012.07.012**.

36 L. Liu, G. Zhang, L. Wang, T. Huang and L. Qin, Highly active S-modified $ZnFe_2O_4$ heterogeneous catalyst and its photo-Fenton behavior under UV-visible irradiation, *Ind. Eng. Chem. Res.*, 2011, **50**(12), 7219–7227, DOI: **10.1021/ie2005516**.

37 Z. Xing, Z. Ju, J. Yang, H. Xu and Y. Qian, One-step hydrothermal synthesis of $ZnFe_2O_4$ nano-octahedrons as a high capacity anode material for Li-ion batteries, *Nano Res.*, 2012, **5**(7), 477–485, DOI: **10.1007/s12274-012-0233-2**.

38 D. Das, A. Mitra, S. Jena, S. B. Majumder and R. N. Basu, Electrophoretically Deposited $ZnFe_2O_4$-Carbon Black Porous Film as a Superior Negative Electrode for Lithium-Ion Battery, *ACS Sustain. Chem. Eng.*, 2018, **6**(12), 17000–17010, DOI: **10.1021/acssuschemeng.8b04332**.

39 Y. Ding, Y. Yang and H. Shao, High capacity $ZnFe_2O_4$ anode material for lithium ion batteries, *Electrochim. Acta*, 2011, **56**(25), 9433–9438, DOI: **10.1016/j.electacta.2011.08.031**.

40 G. Wu, H. Zhang, X. Luo, L. Yang and H. Lv, Investigation and optimization of Fe/$ZnFe_2O_4$ as a Wide-band electromagnetic absorber, *J. Colloid Interface Sci.*, 2019, **536**, 548–555, DOI: **10.1016/j.jcis.2018.10.084**.

41 K. Q. Lu, Y. H. Li, Z. R. Tang and Y. J. Xu, Roles of Graphene Oxide in Heterogeneous Photocatalysis, *ACS Mater. Au*, 2021, **1**(1), 37–54, DOI: **10.1021/acsmaterialsau.1c00022**.

42 A. Razaq, F. Bibi, X. Zheng, R. Papadakis, S. H. M. Jafri and H. Li, Review on Graphene-, Graphene Oxide-, Reduced Graphene Oxide-Based Flexible Composites: From Fabrication to Applications, *Materials*, 2022, **15**(3), 1012, DOI: **10.3390/ma15031012**.

43 M. Al Kausor and D. Chakrabortty, Graphene oxide based semiconductor photocatalysts for degradation of organic dye in waste water: A review on fabrication, performance enhancement and challenges, *Inorg. Chem. Commun.*, 2021, **129**, 108630, DOI: **10.1016/j.inoche.2021.108630**.

44 J. Wu, H. Lin, D. J. Moss, K. P. Loh and B. Jia, Graphene oxide for photonics, electronics and optoelectronics, *Nat. Rev. Chem.*, 2023, **7**, 162–183, DOI: **10.1038/s41570-022-00458-7**.

45 A. Gutiérrez-Cruz, A. R. Ruiz-Hernández, J. F. Vega-Clemente, D. G. Luna-Gazcón and J. Campos-Delgado, A review of top-down and bottom-up synthesis methods for the production of graphene, graphene oxide and reduced graphene oxide, *J. Mater. Sci.*, 2022, **57**, 14543–14578, DOI: **10.1007/s10853-022-07514-z**.

46 R. Abbas, et al., Silver Nanoparticles: Synthesis, Structure, Properties and Applications, *Nanomaterials*, 2024, **14**(17), 1425, DOI: **10.3390/nano14171425**.

47 D. P. Sahoo, S. Patnaik, D. Rath and K. M. Parida, Synergistic effects of plasmon induced Ag@$Ag_3VO_4$/ZnCr LDH ternary heterostructures towards visible light responsive $O_2$ evolution and phenol oxidation reactions, *Inorg. Chem. Front.*, 2018, **5**(4), 879–896, DOI: **10.1039/c7qi00742f**.

48 Y. Tang, et al., Room-temperature $NH_3$ gas sensors based on Ag-doped $\gamma$-$Fe_2O_3$/$SiO_2$ composite films with sub-ppm detection ability, *J. Hazard. Mater.*, 2015, **298**, 154–161, DOI: **10.1016/j.jhazmat.2015.04.044**.

49 P. S. Kolhe, P. M. Koinkar, N. Maiti and K. M. Sonawane, Synthesis of Ag doped $SnO_2$ thin films for the evaluation of $H_2S$ gas sensing properties, *Phys. B*, 2017, **524**, 90–96, DOI: **10.1016/j.physb.2017.07.056**.

50 V. K. Tomer and S. Duhan, A facile nanocasting synthesis of mesoporous Ag-doped $SnO_2$ nanostructures with enhanced humidity sensing performance, *Sens. Actuators, B*, 2016, **223**, 750–760, DOI: **10.1016/j.snb.2015.09.139**.

51 B. Baral, D. P. Sahoo and K. Parida, Discriminatory {040}-Reduction Facet/$Ag^0$ Schottky Barrier Coupled {040/110}-$BiVO_4$@Ag@CoAl-LDH Z-Scheme Isotype Heterostructure, *Inorg. Chem.*, 2021, **60**(3), 1698–1715, DOI: **10.1021/acs.inorgchem.0c03210**.

52 N. Yuangpho, D. T. T. Trinh, D. Channei, W. Khanitchaidecha and A. Nakaruk, The influence of experimental conditions on photocatalytic degradation of methylene blue using titanium dioxide particle, *J. Aust. Ceram. Soc.*, 2018, **54**(3), 557–564, DOI: **10.1007/s41779-018-0184-5**.

53 S. Bibi, et al., Photocatalytic degradation of malachite green and methylene blue over reduced graphene oxide (rGO) based metal oxides (rGO-$Fe_3O_4$/$TiO_2$) nanocomposite under UV-visible light irradiation, *J. Environ. Chem. Eng.*, 2021, **9**(4), 105580, DOI: **10.1016/j.jece.2021.105580**.

54 Y. Zeng, et al., Fabrication of Z-scheme magnetic $MoS_2$/$CoFe_2O_4$ nanocomposites with highly efficient photocatalytic activity, *J. Colloid Interface Sci.*, 2018, **514**, 664–674, DOI: **10.1016/j.jcis.2017.12.079**.

55 S. Li, et al., Fabrication of vessel–like biochar–based heterojunction photocatalyst $Bi_2S_3$/BiOBr/BC for diclofenac removal under visible LED light irradiation: Mechanistic investigation and intermediates analysis, *J. Hazard. Mater.*, 2020, **391**, 121407, DOI: **10.1016/j.jhazmat.2019.121407**.

56 A. Sergejevs, et al., A calibrated UV-LED based light source for water purification and characterisation of photocatalysis, *Photochem. Photobiol. Sci.*, 2017, **16**(11), 1690–1699, DOI: **10.1039/c7pp00269f**.

57 N. Sharma, V. Sharma, Y. Jain, M. Kumari, R. Gupta, S. K. Sharma and K. Sachdev, Synthesis and Characterization of Graphene Oxide (GO) and Reduced Graphene Oxide (rGO) for Gas Sensing Application, *Macromol. Symp.*, 2017, **376**, 1700006.

58 M. Rahman, et al., The X-ray peak profiling, optical and dielectric properties of Ag@$ZnFe_2O_4$/rGO ternary nanocomposites: LED assisted photocatalysis and humidity sensing, *J. Alloys Compd.*, 2024, **984**, 174012, DOI: 10.1016/j.jallcom.2024.174012.

59 M. Venkatesham, D. Ayodhya, A. Madhusudhan and G. Veerabhadram, Synthesis of stable silver nanoparticles using gum acacia as reducing and stabilizing agent and study of its microbial properties: A novel green approach, *Int. J. Green Nanotechnol. Biomed.*, 2012, **4**(3), 199–206, DOI: 10.1080/19430892.2012.705999.

60 H. Kumar Verma, R. C. Srivastava and C. Shekhar Joshi, Synthesis of nickel-cobalt ferrite/graphene oxide nanocomposites, *J. Magn. Magn. Mater.*, 2024, **599**, 172081, DOI: 10.1016/j.jmmm.2024.172081.

61 M. Rahman, et al., The X-ray peak profiling, optical and dielectric properties of Ag@$ZnFe_2O_4$/rGO ternary nanocomposites: LED assisted photocatalysis and humidity sensing, *J. Alloys Compd.*, 2024, **984**, 174012, DOI: 10.1016/j.jallcom.2024.174012.

62 S. G. Prasanna Kumar, et al., Understanding the photoluminescence behaviour in nano $CaZrO_3$:$Eu^{3+}$ pigments by Judd-Ofelt intensity parameters, *Dyes Pigm.*, 2018, **150**, 306–314, DOI: 10.1016/j.dyepig.2017.12.022.

63 U. Holzwarth and N. Gibson, The Scherrer equation versus the 'Debye-Scherrer equation, *Nat. Nanotechnol.*, 2011, **6**(9), 534.

64 M. K. Satheeshkumar, et al., Study of structural, morphological and magnetic properties of Ag substituted cobalt ferrite nanoparticles prepared by honey assisted combustion method and evaluation of their antibacterial activity, *J. Magn. Magn. Mater.*, 2019, **469**, 691–697, DOI: 10.1016/j.jmmm.2018.09.039.

65 M. Basak, M. L. Rahman, M. F. Ahmed, B. Biswas and N. Sharmin, The use of X-ray diffraction peak profile analysis to determine the structural parameters of cobalt ferrite nanoparticles using Debye-Scherrer, Williamson-Hall, Halder-Wagner and Size-strain plot: Different precipitating agent approach, *J. Alloys Compd.*, 2022, **895**, 162694, DOI: 10.1016/j.jallcom.2021.162694.

66 K. V. Zipare, S. S. Bandgar and G. S. Shahane, Effect of Dy-substitution on structural and magnetic properties of Mn–Zn ferrite nanoparticles, *J. Rare Earths*, 2018, **36**(1), 86–94, DOI: 10.1016/j.jre.2017.06.011.

67 S. Debnath, K. Deb, B. Saha and R. Das, X-ray diffraction analysis for the determination of elastic properties of zinc-doped manganese spinel ferrite nanocrystals ($Mn_{0.75}Zn_{0.25}Fe_2O_4$), along with the determination of ionic radii, bond lengths, and hopping lengths, *J. Phys. Chem. Solids*, 2019, **134**, 105–114, DOI: 10.1016/j.jpcs.2019.05.047.

68 V. G. Patil, S. E. Shirsath, S. D. More, S. J. Shukla and K. M. Jadhav, Effect of zinc substitution on structural and elastic properties of cobalt ferrite, *J. Alloys Compd.*, 2009, **488**(1), 199–203, DOI: 10.1016/j.jallcom.2009.08.078.

69 B. A. Patil, J. S. Kounsalye, A. V. Humbe and R. D. Kokate, Structural, magnetic, dielectric and hyperfine interaction studies of titanium ($Ti^{4+}$)-substituted nickel ferrite ($Ni_{1+x}Ti_xFe_{2-2x}O_4$) nanoparticles, *J. Mater. Sci.: Mater. Electron.*, 2021, **32**(4), 4556–4567, DOI: 10.1007/s10854-020-05197-3.

70 M. Bin Mobarak, M. S. Hossain, F. Chowdhury and S. Ahmed, Synthesis and characterization of CuO nanoparticles utilizing waste fish scale and exploitation of XRD peak profile analysis for approximating the structural parameters, *Arabian J. Chem.*, 2022, **15**(10), 104117, DOI: 10.1016/j.arabjc.2022.104117.

71 M. L. Rahman, S. Rahman, B. Biswas, M. F. Ahmed, M. Rahman and N. Sharmin, Investigation of structural, morphological and magnetic properties of nanostructured strontium hexaferrite through co-precipitation technique: Impacts of annealing temperature and Fe/Sr ratio, *Heliyon*, 2023, **9**(3), e14532, DOI: 10.1016/j.heliyon.2023.e14532.

72 K. Sabri, A. Rais, K. Taibi, M. Moreau, B. Ouddane and A. Addou, Structural Rietveld refinement and vibrational study of $MgCr_xFe_{2-x}O_4$ spinel ferrites, *Phys. B*, 2016, **501**, 38–44, DOI: 10.1016/j.physb.2016.08.011.

73 K. M. Srinivasamurthy, et al., Tuning of ferrimagnetic nature and hyperfine interaction of $Ni^{2+}$ doped cobalt ferrite nanoparticles for power transformer applications, *Ceram. Int.*, 2018, **44**(8), 9194–9203, DOI: 10.1016/j.ceramint.2018.02.129.

74 M. Hashim, et al., Synthesis and characterizations of $Ni^{2+}$ substituted cobalt ferrite nanoparticles, *Mater. Chem. Phys.*, 2013, **139**(2–3), 364–374, DOI: 10.1016/j.matchemphys.2012.09.019.

75 F. S. Alruwashid, M. A. Dar, N. H. Alharthi and H. S. Abdo, Effect of graphene concentration on the electrochemical properties of cobalt ferrite nanocomposite materials, *Nanomaterials*, 2021, **11**(10), 2523, DOI: 10.3390/nano11102523.

76 M. K. Satheeshkumar, et al., Study of structural, morphological and magnetic properties of Ag substituted cobalt ferrite nanoparticles prepared by honey assisted combustion method and evaluation of their antibacterial activity, *J. Magn. Magn. Mater.*, 2019, **469**, 691–697, DOI: 10.1016/j.jmmm.2018.09.039.

77 Z. Iqbal, M. S. Tanweer and M. Alam, Reduced Graphene Oxide-Modified Spinel Cobalt Ferrite Nanocomposite: Synthesis, Characterization, and Its Superior Adsorption Performance for Dyes and Heavy Metals, *ACS Omega*, 2023, **8**(7), 6376–6390, DOI: 10.1021/acsomega.2c06636.

78 M. Parastar Gharehlar, S. Sheshmani, F. R. Nikmaram and Z. Doroudi, Synergistic potential in spinel ferrite $MFe_2O_4$ (M = Co, Ni) nanoparticles-mediated graphene oxide: Structural aspects, photocatalytic, and kinetic studies, *Sci. Rep.*, 2024, **14**(1), 4625, DOI: 10.1038/s41598-024-55452-4.

79 N. Ambikeswari and S. Manivannan, Superior magnetodielectric properties of room temperature

synthesized superparamagnetic cobalt ferrite – graphene oxide composite, *J. Alloys Compd.*, 2018, **763**, 711–718, DOI: 10.1016/j.jallcom.2018.05.275.

80 W. Tahir, et al., Impact of silver substitution on the structural, magnetic, optical, and antibacterial properties of cobalt ferrite, *Sci. Rep.*, 2023, **13**(1), 15730, DOI: 10.1038/s41598-023-41729-7.

81 H. Kumar Verma, R. C. Srivastava and C. Shekhar Joshi, Synthesis of nickel-cobalt ferrite/graphene oxide nanocomposites, *J. Magn. Magn. Mater.*, 2024, **599**, 172081, DOI: 10.1016/j.jmmm.2024.172081.

82 M. A. M. Khan, W. Khan, M. Ahamed, J. Ahmed, M. A. Al-Gawati and A. N. Alhazaa, Silver-Decorated Cobalt Ferrite Nanoparticles Anchored onto the Graphene Sheets as Electrode Materials for Electrochemical and Photocatalytic Applications, *ACS Omega*, 2020, **5**(48), 31076–31084, DOI: 10.1021/acsomega.0c04191.

83 N. Dhanda, P. Thakur, A. C. Aidan Sun and A. Thakur, Structural, optical and magnetic properties along with antifungal activity of Ag-doped Ni-Co nanoferrites synthesized by eco-friendly route, *J. Magn. Magn. Mater.*, 2023, **572**, 170598, DOI: 10.1016/j.jmmm.2023.170598.

84 Y. Fu, H. Chen, X. Sun and X. Wang, Combination of cobalt ferrite and graphene: High-performance and recyclable visible-light photocatalysis, *Appl. Catal., B*, 2012, **111–112**, 280–287, DOI: 10.1016/j.apcatb.2011.10.009.

85 N. Kaur and M. Kaur, Envisioning the composition effect on structural, magnetic, thermal and optical properties of mesoporous $MgFe_2O_4$-GO nanocomposites, *Ceram. Int.*, 2018, **44**(4), 4158–4168, DOI: 10.1016/j.ceramint.2017.11.217.

86 M. F. Elmahaishi, R. S. Azis, I. Ismail and F. D. Muhammad, A review on electromagnetic microwave absorption properties: their materials and performance, *J. Mater. Res. Technol.*, 2022, **20**, 2188–2220, DOI: 10.1016/j.jmrt.2022.07.140.

87 Y. Fu, H. Chen, X. Sun and X. Wang, Combination of cobalt ferrite and graphene: High-performance and recyclable visible-light photocatalysis, *Appl. Catal., B*, 2012, **111–112**, 280–287, DOI: 10.1016/j.apcatb.2011.10.009.

88 M. A. M. Khan, W. Khan, M. Ahamed, J. Ahmed, M. A. Al-Gawati and A. N. Alhazaa, Silver-Decorated Cobalt Ferrite Nanoparticles Anchored onto the Graphene Sheets as Electrode Materials for Electrochemical and Photocatalytic Applications, *ACS Omega*, 2020, **5**(48), 31076–31084, DOI: 10.1021/acsomega.0c04191.

89 N. Dhanda, P. Thakur, A. C. Aidan Sun and A. Thakur, Structural, optical and magnetic properties along with antifungal activity of Ag-doped Ni-Co nanoferrites synthesized by eco-friendly route, *J. Magn. Magn. Mater.*, 2023, **572**, 170598, DOI: 10.1016/j.jmmm.2023.170598.

90 A. Redinger and S. Siebentritt, Loss Mechanisms in Kesterite Solar Cells, *Copper Zinc Tin Sulfide-Based Thin-Film Sol. Cells*, 2015, **627**, 363–386, DOI: 10.1002/9781118437865.ch16.

91 H. Fu, S. Zhang, T. Xu, Y. Zhu and J. Chen, Photocatalytic degradation of RhB by fluorinated $Bi_2WO_6$ and distributions of the intermediate products, *Environ. Sci. Technol.*, 2008, **42**(6), 2085–2091, DOI: 10.1021/es702495w.

92 R. Pandit, K. K. Sharma, P. Kaur and R. Kumar, Cation distribution controlled dielectric, electrical and magnetic behavior of $In^{3+}$ substituted cobalt ferrites synthesized via solid-state reaction technique, *Mater. Chem. Phys.*, 2014, **148**(3), 988–999, DOI: 10.1016/j.matchemphys.2014.09.009.

93 R. S. Devan and B. K. Chougule, Effect of composition on coupled electric, magnetic, and dielectric properties of two phase particulate magnetoelectric composite, *J. Appl. Phys.*, 2007, **101**(1), 014109, DOI: 10.1063/1.2404773.

94 P. N. Anantharamaiah, et al., Tunable Dielectric Properties of Nickel Ferrite Derived via Crystallographic Site Preferential Cation Substitution, *J. Phys. Chem. C*, 2022, **126**(21), 9123–9134, DOI: 10.1021/acs.jpcc.2c00529.

95 P. Chavan, L. R. Naik, P. B. Belavi, G. Chavan, C. K. Ramesha and R. K. Kotnala, Studies on Electrical and Magnetic Properties of Mg-Substituted Nickel Ferrites, *J. Electron. Mater.*, 2017, **46**(1), 188–198, DOI: 10.1007/s11664-016-4886-6.

96 R. C. Kambale, P. A. Shaikh, C. H. Bhosale, K. Y. Rajpure and Y. D. Kolekar, The effect of Mn substitution on the magnetic and dielectric properties of cobalt ferrite synthesized by an autocombustion route, *Smart Mater. Struct.*, 2009, **18**(11), 115028, DOI: 10.1088/0964-1726/18/11/115028.

97 A. Naz, et al., Cu and Fe doped $NiCo_2O_4$/g-$C_3N_4$ nanocomposite ferroelectric, magnetic, dielectric and optical properties: Visible light-driven photocatalytic degradation of RhB and CR dyes, *Diamond Relat. Mater.*, 2024, **141**, 110592, DOI: 10.1016/j.diamond.2023.110592.

98 S. Pareek and J. K. Quamara, Dielectric and optical properties of graphitic carbon nitride–titanium dioxide nanocomposite with enhanced charge separation, *J. Mater. Sci.*, 2018, **53**(1), 604–612, DOI: 10.1007/s10853-017-1506-7.

99 Meena and A. Sharma, Dielectric spectroscopy of Ag-starch nanocomposite films, *Mater. Res. Express*, 2018, **5**(4), 045041, DOI: 10.1088/2053-1591/aabcd6.

100 P. A. Shaikh, R. C. Kambale, A. V. Rao and Y. D. Kolekar, Structural, magnetic and electrical properties of Co-Ni-Mn ferrites synthesized by co-precipitation method, *J. Alloys Compd.*, 2010, **492**(1–2), 590–596, DOI: 10.1016/j.jallcom.2009.11.189.

101 S. Mahalakshmi, K. SrinivasaManja and S. Nithiyanantham, Electrical Properties of Nanophase Ferrites Doped with Rare Earth Ions, *J. Supercond. Novel Magn.*, 2014, **27**(9), 2083–2088, DOI: 10.1007/s10948-014-2551-y.

102 I. H. Gul and A. Maqsood, Structural, magnetic and electrical properties of cobalt ferrites prepared by the sol-gel route, *J. Alloys Compd.*, 2008, **465**(1–2), 227–231, DOI: 10.1016/j.jallcom.2007.11.006.

103 X. Zhou, et al., Template-free synthesis of hierarchical $ZnFe_2O_4$ yolk-shell microspheres for high-sensitivity acetone sensors, *Nanoscale*, 2016, **8**(10), 5446–5453, DOI: 10.1039/c5nr06308f.

104 A. Kheradmand, A. Wainwright, L. Wang and Y. Jiang, Anchoring Iron Oxides on Carbon Nitride Nanotubes for Improved Photocatalytic Hydrogen Production, *Energy Fuels*, 2021, **35**(1), 868–876, DOI: **10.1021/acs.energyfuels.0c03901**.

105 L. Sun, R. Shao, L. Tang and Z. Chen, Synthesis of $ZnFe_2O_4$/ZnO nanocomposites immobilized on graphene with enhanced photocatalytic activity under solar light irradiation, *J. Alloys Compd.*, 2013, **564**, 55–62, DOI: **10.1016/j.jallcom.2013.02.147**.

106 L. Gan, L. Xu and K. Qian, Preparation of core-shell structured $CoFe_2O_4$ incorporated $Ag_3PO_4$ nanocomposites for photocatalytic degradation of organic dyes, *Mater. Des.*, 2016, **109**, 354–360, DOI: **10.1016/j.matdes.2016.07.043**.

107 A. H. Mady, M. L. Baynosa, D. Tuma and J. J. Shim, Facile microwave-assisted green synthesis of Ag-$ZnFe_2O_4$@rGO nanocomposites for efficient removal of organic dyes under UV- and visible-light irradiation, *Appl. Catal., B*, 2017, **203**, 416–427, DOI: **10.1016/j.apcatb.2016.10.033**.

108 Y. Cheng, et al., Review on spinel ferrites-based materials ($MFe_2O_4$) as photo-Fenton catalysts for degradation of organic pollutants, *Sep. Purif. Technol.*, 2023, **318**, 123971, DOI: **10.1016/j.seppur.2023.123971**.

109 H. S. Jarusheh, A. Yusuf, F. Banat, M. A. Haija and G. Palmisano, Integrated photocatalytic technologies in water treatment using ferrites nanoparticles, *J. Environ. Chem. Eng.*, 2022, **10**(5), 108204, DOI: **10.1016/j.jece.2022.108204**.

110 H. Saeed, et al., Mixed metal ferrite ($Mn_{0.6}Zn_{0.4}Fe_2O_4$) intercalated g-$C_3N_4$ nanocomposite: Efficient sunlight driven photocatalyst for methylene blue degradation, *Nanotechnology*, 2021, **32**(50), 505714, DOI: **10.1088/1361-6528/ac2847**.

111 R. Jasrotia, N. Jaswal, J. Prakash, C. C. Kit, J. Singh and A. Kandwal, Photocatalytic application of magnesium spinel ferrite in wastewater remediation: A review, *J. Magnesium Alloys*, 2024, **12**(2), 490–505, DOI: **10.1016/j.jma.2024.02.006**.

112 R. Acharya, S. Pati and K. Parida, A review on visible light driven spinel ferrite-g-$C_3N_4$ photocatalytic systems with enhanced solar light utilization, *J. Mol. Liq.*, 2022, **357**, 119105, DOI: **10.1016/j.molliq.2022.119105**.

113 K. K. Das, S. Mansingh, R. Mohanty, D. P. Sahoo, N. Priyadarshini and K. Parida, 0D-2D $Fe_2O_3$/Boron-Doped g-$C_3N_4$ S-Scheme Exciton Engineering for Photocatalytic $H_2O_2$ Production and Photo-Fenton Recalcitrant-Pollutant Detoxification: Kinetics, Influencing Factors, and Mechanism, *J. Phys. Chem. C*, 2023, **127**(1), 22–40, DOI: **10.1021/acs.jpcc.2c06369**.

114 S. Mansingh, K. Kumar Das, R. Mohanty, N. Priyadarshini and K. Parida, Inverse opal type porous g-$C_3N_4$ towards $H_2O_2$ production and in-situ photoFenton gemifloxacin degradation driven by amorphous framework and nitrogen vacancy, *Appl. Catal., A*, 2025, **693**, 120141, DOI: **10.1016/j.apcata.2025.120141**.

115 M. Saquib, R. Kaushik and A. Halder, Photoelectrochemical Activity of Ag Coated 2D-$TiO_2$/RGO Heterojunction for Hydrogen Evolution Reaction and Environmental Remediation, *ChemistrySelect*, 2020, **5**(21), 6376–6388, DOI: **10.1002/slct.202000843**.

116 R. Beura, R. Pachaiappan and T. Paramasivam, Photocatalytic degradation studies of organic dyes over novel Ag-loaded ZnO-graphene hybrid nanocomposites, *J. Phys. Chem. Solids*, 2021, **148**, 109689, DOI: **10.1016/j.jpcs.2020.109689**.

117 G. Varsha Raj, H. N. Priyadarshini, K. Prashantha, G. Nagaraju, Udayabhanu and T. Ramakrishnappa, Green synthesis of Ag-$ZnFe_2O_4$@graphene nanocomposite for photocatalytic and electrochemical applications, *Opt. Mater.*, 2024, **147**, 114704, DOI: **10.1016/j.optmat.2023.114704**.